CrossMark

A new troubled-cell indicator for discontinuous Galerkin methods for hyperbolic conservation laws

Guosheng Fu, Chi-Wang Shu [*],[1]

Division of Applied Mathematics, Brown University, Providence, RI 02912, USA

ABSTRACT

We introduce a new troubled-cell indicator for the discontinuous Galerkin (DG) methods for solving hyperbolic conservation laws. This indicator can be defined on unstructured meshes for high order DG methods and depends only on data from the target cell and its immediate neighbors. It is able to identify shocks without PDE sensitive parameters to tune. Extensive one- and two-dimensional simulations on the hyperbolic systems of Euler equations indicate the good performance of this new troubled-cell indicator coupled with a simple minmod-type TVD limiter for the Runge–Kutta DG (RKDG) methods.

© 2017 Elsevier Inc. All rights reserved.

1. Introduction

In this paper, we introduce a new troubled-cell indicator for the discontinuous Galerkin methods for solving hyperbolic conservation laws.

The first discontinuous Galerkin (DG) method was introduced in 1973 by Reed and Hill [18], in the framework of neutron transport (steady state linear hyperbolic equations). A major development of the DG method was carried out by Cockburn et al. in a series of papers [6,5,4,3,7], in which they established a framework to easily solve *nonlinear* time dependent hyperbolic conservation laws:

$$\begin{cases} u_t + \nabla \cdot f(u) = 0 \\ u(\pmb{x}, 0) = u_0(\pmb{x}) \end{cases} \tag{1.1}$$

using explicit, nonlinearly stable high order Runge–Kutta time discretization [21] and DG discretization in space with exact or approximate Riemann solvers as interface fluxes and a total variation bounded (TVB) limiter [20] to achieve non-oscillatory properties for strong shocks. These schemes are termed RKDG methods.

An important component of RKDG methods for solving conservation laws (1.1) with strong shocks in the solutions is a nonlinear limiter, which is applied to detect discontinuities and control spurious oscillations near such discontinuities. Early examples of such limiters are the minmod type TVB limiter [6,5,4,3,7], and the moment based limiters [1,2]. These limiters do control the oscillations well, however they may degrade accuracy when mistakenly used in smooth regions of the solution, especially for high-order polynomial degrees. More recently, weighted essentially non-oscillatory (WENO) limiters [17,14,16,34,33,36,37,35] were introduced which can achieve both high-order accuracy and non-oscillatory properties. The

---

* Corresponding author.
  E-mail addresses: guosheng_fu@brown.edu (G. Fu), shu@dam.brown.edu (C.-W. Shu).
[1] Research supported by ARO grant W911NF-15-1-0226 and NSF grant DMS-1418750.

WENO limiters are constructed by first (Step 1) identify the "troubled cells", namely those cells which might need the limiting procedure, through a troubled-cell indicator, and then (Step 2) replace the solution polynomials in those troubled cells by reconstructed polynomials using certain WENO methodology which maintain the original cell average (conservation), have the same orders of accuracy as before, but are less oscillatory.

In [15], various discontinuity detecting methods were systematically studied and compared as troubled-cell indicators for the WENO limiter for RKDG methods for the compressible Euler equations. While they found no universally better indicator for every problem, the minmod type TVB indicator [5,20] with a suitably chosen constant, Harten's subcell resolution idea [9], and the shock detector of Krivodonova et al. (KXRCF) [12] performed better than other methods. More recently, an alternative family of DG limiters which serves at the same time as a new PDE-based limiter, as well as a troubled-cell indicator, was introduced by Dumbser et al. [8]. The multiwavelet troubled-cell indicator was introduced by Vuik and Ryan [24], and later the same authors used automated parameter selection based on Tukey's boxplot approach [23] to automatically determine the tuning parameter for various troubled-cell indicators [25].

In this paper, we introduce a new reliable and efficient high-order troubled-cell indicator for the DG methods on unstructured grids without PDE-sensitive parameters to tune. The indicator, depending only on the polynomial in the target cell and its immediate neighbors, is formally $(k+1)$-th order small in smooth regions for DG-$\mathcal{P}_k$, and is of $\mathcal{O}(1)$ near shocks. This nice separation of the indicator in smooth regions and shocks ensures that cells in smooth regions will not be marked as troubled cells. We demonstrate the robust performance of our indicator, coupled with the minmod-type TVD limiter [4,7] for the RKDG methods, for various numerical tests for the compressible Euler equations in 1D and 2D. We remark that the TVD limiter may not be the best limiter to use in the troubled cells, however the focus of this paper is on the troubled-cell indicators, not on limiters used in these troubled cells.

The rest of the paper is outlined as follows. In Section 2, we briefly review the RKDG method, and then present the new troubled-cell indicator. In Section 3, we provide extensive numerical results in 1D and 2D for the compressible Euler equations to show the good performance of the new troubled-cell indicator. And we conclude in Section 4.

2. New troubled-cell indicator for the RKDG method

In this section, we first briefly review the RKDG method for solving the conservation law (1.1). Then, we present the new troubled-cell indicator to identify troubled cells. The minmod-type TVD limiter [4,7] is then used on these troubled cells.

2.1. Review of the RKDG methods

In this subsection, we give a brief review of the RKDG methods for solving conservation laws (1.1) in two dimensions.

We first use the DG method to discretize the spatial variables. Given a triangulation of the computational domain consisting of cells Δ_j, the DG method has its solution as well as the test function space given by $V_h^k = \{v(x, y) : v(x, y)|_{\Delta_j} \in \mathcal{P}^k(\Delta_j)\}$, where $\mathcal{P}^k(\Delta_j)$ denotes the set of polynomials of degree at most k defined on Δ_j. The semi-discrete DG method for solving (1.1) is defined as follows: find the unique function $u_h \in V_h^k$, such that

$$\int_{\Delta_j} (u_h)_t \, v \, dxdy = \int_{\Delta_j} f(u_h) \cdot \nabla v \, dxdy - \int_{\partial \Delta_j} \widehat{f(u_h)} \cdot n \, v ds \tag{2.1}$$

holds on all cells Δ_j, for all the test functions $v \in V_h^k$. Here $n = (n_x, n_y)^T$ is the outward unit normal of the triangle boundary $\partial \Delta_j$, and $\widehat{f(u_h)} \cdot n$ is a monotone numerical flux for the scalar case and an exact or approximate Riemann solver for the system case. The local Lax–Friedrichs flux [5] is used in all of our numerical tests.

The semi-discrete scheme (2.1) can be written as

$$u_t = L(u),$$

where $L(u)$ is the spatial discretization operator. We discretize it in time by a non-linearly stable Runge–Kutta time discretization [21], e.g. the third-order version:

$$
\begin{aligned}
u^{(1)} &= u^n + \Delta t L(u^n), \\
u^{(2)} &= \frac{3}{4} u^n + \frac{1}{4} u^{(1)} + \frac{1}{4} \Delta t L(u^{(1)}), \\
u^{n+1} &= \frac{1}{3} u^n + \frac{2}{3} u^{(2)} + \frac{2}{3} \Delta t L(u^{(2)}).
\end{aligned}
\tag{2.2}
$$

2.2. The troubled-cell indicator

Here we introduce the new troubled-cell indicator for the RKDG method (2.1), (2.2). We first relabel the target cell as Δ_0, and denote the indicator stencil as $S = \{\Delta_0, \Delta_1, \Delta_2, \Delta_3\}$ as shown in Fig. 2.1. We then denote the DG-$\mathcal{P}_k$ solutions on these four cells as $p_\ell(x, y), \ell = 0, 1, 2, 3$, respectively. We consider the following quantity defined on each target cell
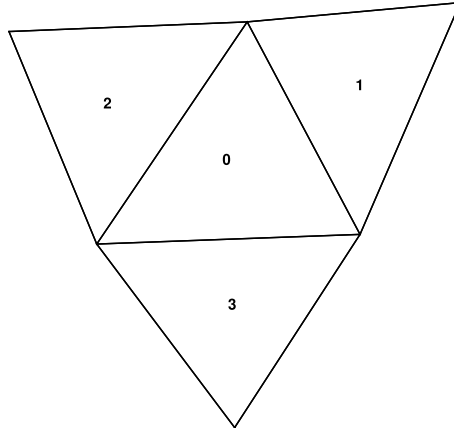
Fig. 2.1. The stencil $S = \{\Delta_0, \Delta_1, \Delta_2, \Delta_3\}$.

$$I_{\Delta_0} := \frac{\sum_{j=1}^{3} |\bar{\bar{p}}_0 - \bar{\bar{p}}_j|}{\max_{j \in \{0,1,2,3\}} \{|\bar{p}_j|\}}, \tag{2.3}$$

where

$$\bar{\bar{p}}_j = \frac{1}{\Delta_0} \int_{\Delta_0} p_j(x, y) \, dxdy, \quad \bar{p}_j = \frac{1}{\Delta_j} \int_{\Delta_j} p_j(x, y) \, dxdy,$$

i.e., $\bar{\bar{\star}}$ denotes the cell average of the function $\star$ on the target cell while $\bar{\star}$ denotes the cell average of the function $\star$ on its own associated cell. Note that, in order to evaluate $\bar{\bar{p}}_\ell$ for $\ell = 1, 2, 3$, the polynomial data $p_\ell(x, y)$ on the neighboring cells are *naturally* extrapolated to the target cell Δ_0. The target cell Δ_0 is treated as a troubled cell if

$$I_{\Delta_0} > C_k \tag{2.4}$$

for a constant C_k that depends only on the polynomial degree k.

Remark 2.1. The indicating quantity (2.3) is defined on any structured/unstructured mesh in any space dimension, with the summation on the numerator over immediate neighbors of the target cell. Note that if Δ_0 is a d-dimensional simplex, the indicating quantity is $I_{\Delta_0} = \frac{\sum_{j=1}^{d+1} |\bar{\bar{p}}_0 - \bar{\bar{p}}_j|}{\max_{j \in \{0,1,\cdots,d\}} \{|\bar{p}_j|\}}$ since a simplicial cell has $d + 1$ immediate neighbors. The computation of this indicating quantity is relatively inexpensive since it only depends on the cell averages and the extended cell averages of the target cell and its immediate neighbors.

Remark 2.2. In smooth regions, the DG-$\mathcal{P}_k$ solution without limiter is formally $(k + 1)$-th order accurate, so both $\bar{\bar{p}}_0$ and $\bar{\bar{p}}_j$ are formally $(k + 1)$-th order approximation to the same cell average of the exact solution. Therefore, we expect the quantity $|\bar{\bar{p}}_0 - \bar{\bar{p}}_j|$, and hence I_{Δ_0}, to be of the size $\mathcal{O}(h^{k+1})$ in smooth regions, where h stands for the mesh size. Near shocks, the quantity $|\bar{\bar{p}}_0 - \bar{\bar{p}}_j|$, and hence I_{Δ_0}, is expected to behave wildly, resulting in an $\mathcal{O}(1)$ value, which is expected to be larger for higher polynomial degree due to the oscillatory nature of high order polynomials. The denominator in (2.3) ensure the indicating quantity is dimensionless.

In the next section, we compare numerical results using this new indicator with one of the best troubled-cell indicators found in [15], namely, the following KXRCF indicator [12]. The indicating quantity for KXRCF is

$$I_{\Delta_0}^{KXRCF} := \frac{\left| \int_{\partial \Delta_0^-} p(x, y)|_{\Delta_0} - p(x, y)|_{\Delta_\ell} \, ds \right| / |\partial \Delta_0^-|}{h^{\frac{k+1}{2}} \| p(x, y)|_{\Delta_0} \|_{\Delta_0}}, \tag{2.5}$$

and a cell is marked as troubled cell if $I_{\Delta_0}^{KXRCF} > \mathsf{C}_k$, where C_k is usually taken to be 1. Here $\partial \Delta_0^-$ denotes the inflow part of the boundary of the cell Δ_0, and Δ_ℓ the neighboring cells sharing the edge(s) in $\partial \Delta_0^-$. The mesh size h is taken to be the radius of the circumscribed circle on Δ_0, and the norm in the denominator is a maximum norm based on local solution maxima at integration points in two dimensions and a cell average in one dimension.

We note that both numerators of (2.3) and (2.5) are formally $\mathcal{O}(h^{k+1})$ in smooth regions and order $\mathcal{O}(1)$ near discontinuities. However, the numerator of (2.3) is observed to be significantly larger (might be orders of magnitude larger) than that of (2.5) for high order polynomials due to the oscillatory nature of high order polynomials, which results in a larger gap of the indicating quantity between smooth regions and discontinuities.

Also, we note that, due to the scaling of $h^{(k+1)/2}$ in the denominator, the KXRCF indicator tends to mark a lot more troubled cells than necessary for high-order DG methods. In our 1D numerical results in the next section, we decrease the power of h in the denominator of (2.5) to be $\frac{\min\{k,2\}+1}{2}$, which seems to be strong enough to single out discontinuities.

2.3. The minmod-type limiter

After identifying the troubled cells by a troubled cell indicator, we are ready to apply limiters for the solution in the troubled cells. We choose to take the characteristic-wise minmod-type limiter on the troubled cells (with the TVB constant M taken to be 0); see details of the limiter in [4] for 1D systems, and in [7] for 2D systems on triangular grids. Note that the limiter does not change the cell averages for conservation.

3. Numerical results

In this section, we perform extensive numerical experiments for 1D and 2D compressible Euler systems to investigate the effectiveness of the new troubled-cell indicator.

In our 1D simulations, we compare the results with a slightly modified KXRCF indicator [12] where the power of h in the denominator is taken as $\frac{\min\{k,2\}+1}{2}$. We detect an element as troubled if it is detected by either density or energy. The constant C_k for the KXRCF indicator is taken as 1 in all tests. The original KXRCF indicator marks a lot more troubled cells than this modified one for $k = 4, 6$; for this reason, we do not report results using the original KXRCF indicator. The constant C_k for our new indicator is taken as 0.1 for $k = 2$, 0.5 for $k = 4$, and 5 for $k = 6$ in all our 1D tests, and is taken as $0.015 \times 2^{k-1}$ or $0.03 \times 2^{k-1}$ for $k = 1, 2, 3$ in our 2D tests. We note that similar results for the 1D simulations using odd polynomial degrees $k = 1, 3, 5$ (with constant C_k being 0.05, 0.25, 2.5, respectively) are obtained, but only results for even degrees $k = 2, 4, 6$ are reported to save space.

Remark 3.1. As is true for most troubled-cell indicators, taking the threshold constant too small would mark more troubled cells than necessary, especially for the cells near a shock, while taking it too big would leads to missed shocks. Here we show numerically that a good choice of the constant C_k for the new indicator is insensitive to a particular test case, while it only depends strongly on the polynomial degree. We tune the constant C_k via test-and-trial for a specific test (Example 3.1 below in 1D, and Example 3.9 in 2D) on a relative coarse mesh. As shown in the numerical experiments below, for a given polynomial degree, a fixed choice of constant C_k works well for all tests considered in this section.

Since the limiter does not guarantee the positivity of density and/or pressure, we also add a positivity preserving limiter [29,30,32] whenever a negative cell average of density or pressure is observed. We use a similar implementation as suggested in [26] for the Euler equations with chemical reactions and in [28] for the compressible Navier–Stokes equations to incorporate the positivity-preserving limiter.

The implementation flow chart is given as follows:

(1.) Use SSP Runge–Kutta time discretization. The third-order version (2.2) is used for $k \geq 2$ in all the numerical tests, and a second-order version is used for $k = 1$ in our 2D tests.
(2.) Use DG-$\mathcal{P}_k$ spatial discretization (2.1) with a local Lax–Friedrichs flux. We run simulations for $\mathcal{P}_2$, $\mathcal{P}_4$ and $\mathcal{P}_6$ in 1D and $\mathcal{P}_1$, $\mathcal{P}_2$ and $\mathcal{P}_3$ in 2D. We take the CFL number to be 0.3 for $\mathcal{P}_1$, 0.15 for $\mathcal{P}_2$, 0.1 for $\mathcal{P}_3$, 0.06 for $\mathcal{P}_4$, and 0.03 for $\mathcal{P}_6$.
(3.) In each stage of the Runge–Kutta time discretization, monitor the cell averages of density and pressure. If a negative cell average appears, redo the whole computation by halving the time step, and applying the following Steps 3.1–3.3. If no negative cell average is obtained, apply the following Steps 3.1–3.2.
  (3.1.) Fix a threshold C_k in the troubled-cell indicator (2.4) for a given polynomial degree k. Apply the indicator (2.4) with both density and total energy as the indicating variable. Take the troubled cells as the union of those obtained from these two indicating variables.
  (3.2.) Apply the characteristic-wise minmod-type limiter [4,7] on the troubled cells.
  (3.3.) Apply the positivity-preserving limiter [31].

Note that the positivity-preserving limiter is only activated if a negative pressure/density cell average is observed.

3.1. 1D tests

We solve the 1D Euler equations (1.1) with

$$u = (\rho, \rho\mu, E)^T, \qquad f(u) = (\rho\mu, \rho\mu^2 + p, \mu(E + p))^T.$$
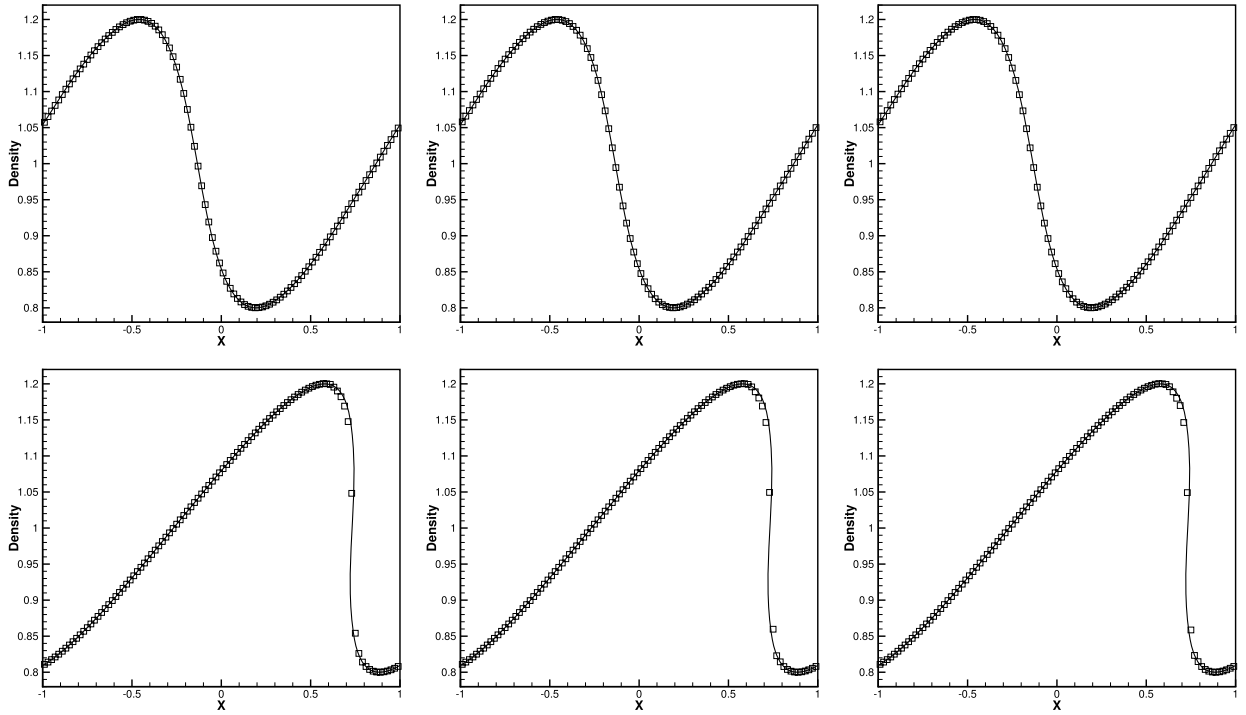
Fig. 3.1. Smooth test. Left: $k = 2$; middle: $k = 4$; right: $k = 6$. Top: $t = 0.25$; bottom: $t = 0.5$. Solid line: the exact solution; Squares: numerical solution. 100 cells. One point per cell is plotted.

Here ρ is the density, μ is the velocity, E is the total energy, and p is the pressure, related to the total energy by $E = \frac{p}{\gamma-1} + \frac{1}{2}\rho\mu^2$.

Example 3.1. We consider a non-physical smooth test. We take $\gamma = 3$. The initial conditions are:

$$\rho(x, 0) = 1 + 0.2\sin(\pi x), \quad \mu(x, 0) = \sqrt{\gamma}\rho(x, 0), \quad p(x, 0) = \rho(x, 0)^\gamma.$$

The computational domain is $x \in [-1, 1]$. Periodic boundary conditions are applied in this test. By the choice of γ and the initial conditions, it is easy to verify that the exact solution for density is nothing but the solution for the following scalar Burgers equation:

$$v_t + (\sqrt{\gamma}v^2)_x = 0$$

with initial condition $v(x, 0) = 1 + 0.2\sin(\pi x)$, and the velocity and pressure satisfies $\mu = \sqrt{\gamma}\rho$, and $p = \rho^\gamma$. For the above initial condition, the solution is smooth up to time $T = \frac{5\sqrt{3}}{6\pi} \approx 0.46$. We compute the solution up to time $t = 0.5$. The computed densities ρ are plotted at time $t = 0.25$ and $t = 0.5$ against the exact solution in Fig. 3.1 for polynomial degree $k = 2, 4, 6$ on $N = 100$ uniform cells. The indicator value $I_\Delta := \max\{I_\Delta(\rho), I_\Delta(E)\}$ at time $t = 0.25$ and $t = 0.5$, along with the time history of the troubled cells are shown in Fig. 3.2. It is clear from Fig. 3.2 that no limiter is activated at time $t = 0.25$, and the indicator is indeed high-order for smooth data.

Example 3.2. We use the following Riemann initial condition for the Sod problem:

$$(\rho, v, p) = (1, 0, 1) \text{ for } x \in [-5, 0]; \qquad (\rho, v, p) = (0.125, 0, 0.1) \text{ for } x \in (0, 5].$$

Average (over time) and maximum percentages of cells being flagged as troubled cells for the new and KXRCF indicators, are summarized in Table 3.1 for $t = 2.0$ using $N = 200$ and $N = 400$ uniform cells. We observe from Table 3.1 that the percentage of troubled cells gets reduced by about a half with a mesh refinement for the new indicator, which is a desired property of the troubled cell indicator. On the other hand, the KXRCF indicator tends to mark more cells on average when the mesh is refined. We do notice that the new indicator tends to detect more cells if the polynomial degree k is higher, while the KXRCF indicator tends to detect fewer cells with an increasing k, which is more desirable.
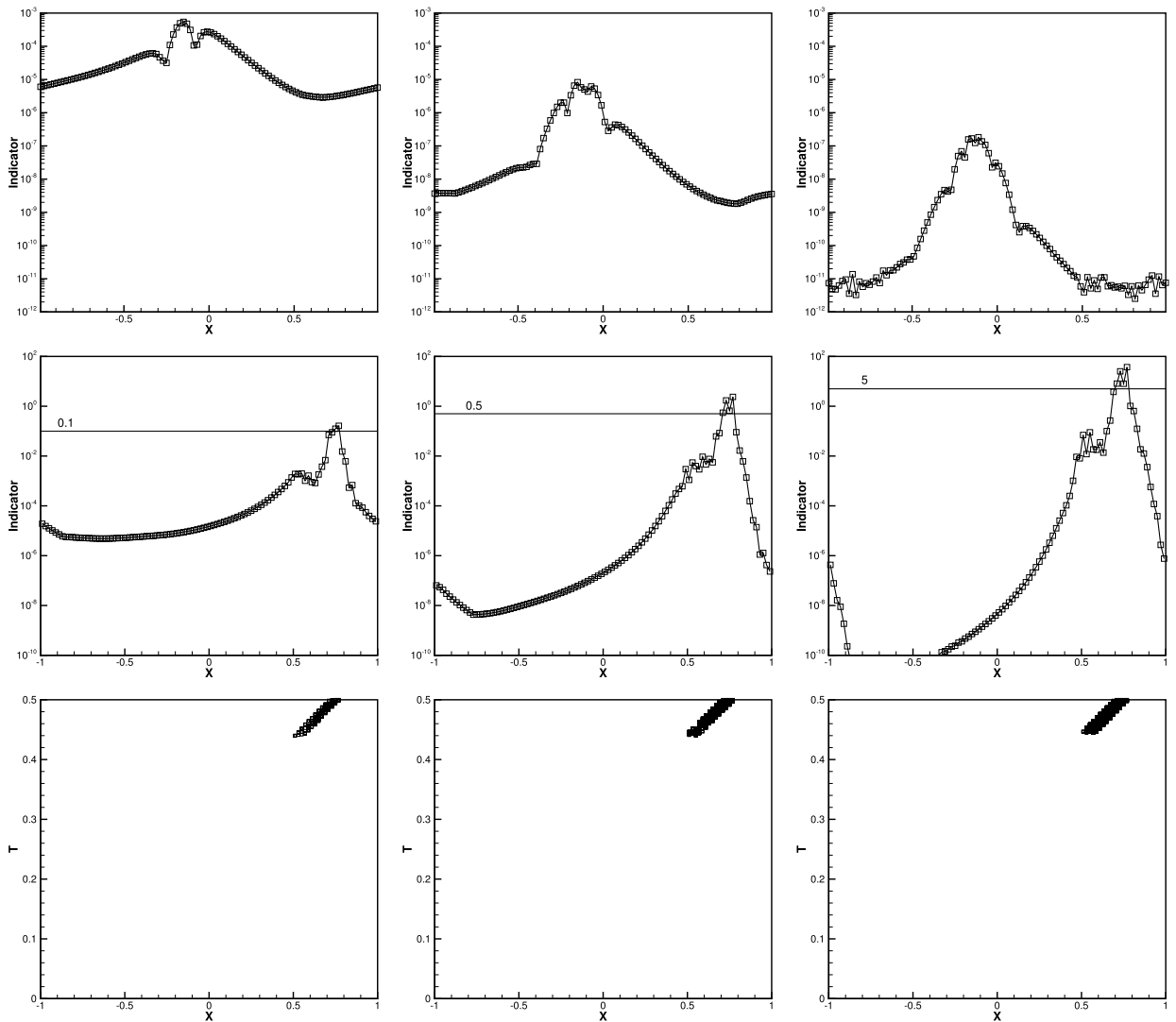
Fig. 3.2. Smooth test. Left: $k = 2$; middle: $k = 4$; right: $k = 6$. Top row: I_Δ at $t = 0.25$; middle row: I_Δ at $t = 0.5$; bottom row: Troubled cells (denoted by squares). 100 cells.
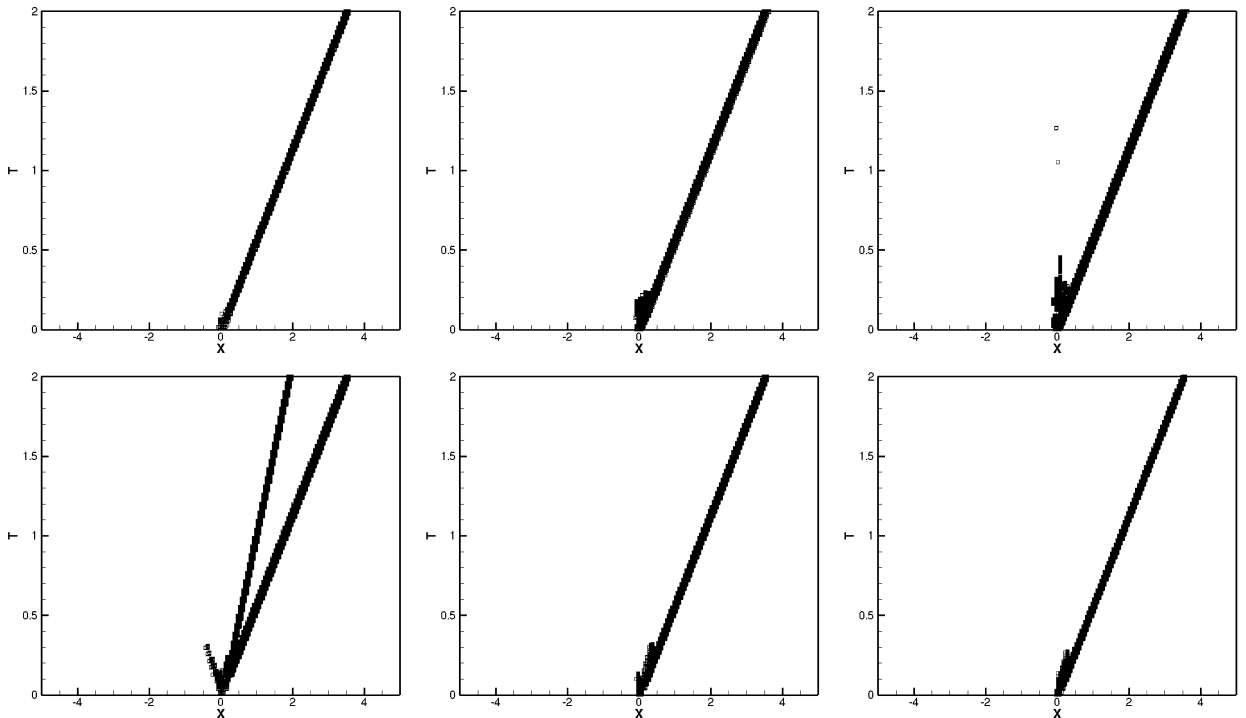
Table 3.1
Average and maximum percentages of cells flagged as troubled cells subject to different troubled-cell indicators for the Sod problem.

| N	Schemes	$\mathcal{P}_2$		$\mathcal{P}_4$		$\mathcal{P}_6$	
	Indicator	Ave	Max	Ave	Max	Ave	Max
200	new	1.38	2.50	1.67	4.00	1.95	5.00
	KXRCF	3.09	5.00	1.66	3.50	1.41	3.00
400	new	0.69	1.25	0.81	2.00	0.91	2.50
	KXRCF	2.41	3.75	1.81	2.50	1.47	2.50

In Fig. 3.3, we plot the computed densities ρ at $t = 2.0$ against the exact solution with $N = 200$ uniform cells for $k = 2$, 4 and 6 using both indicators. The time history of the troubled cells for both indicators are shown in Fig. 3.4. We see that contact discontinuities are initially marked as troubled cells for both indicators for all polynomial degrees, but are left out after a few steps (except for the KXRCF indicator for $k = 2$ where they continue to be marked as troubled cells) possibly due to the smearing of the DG solution. Similar results are obtained for both indicators. We can observe that the results for all cases keep sharp discontinuities and are mostly oscillation-free.
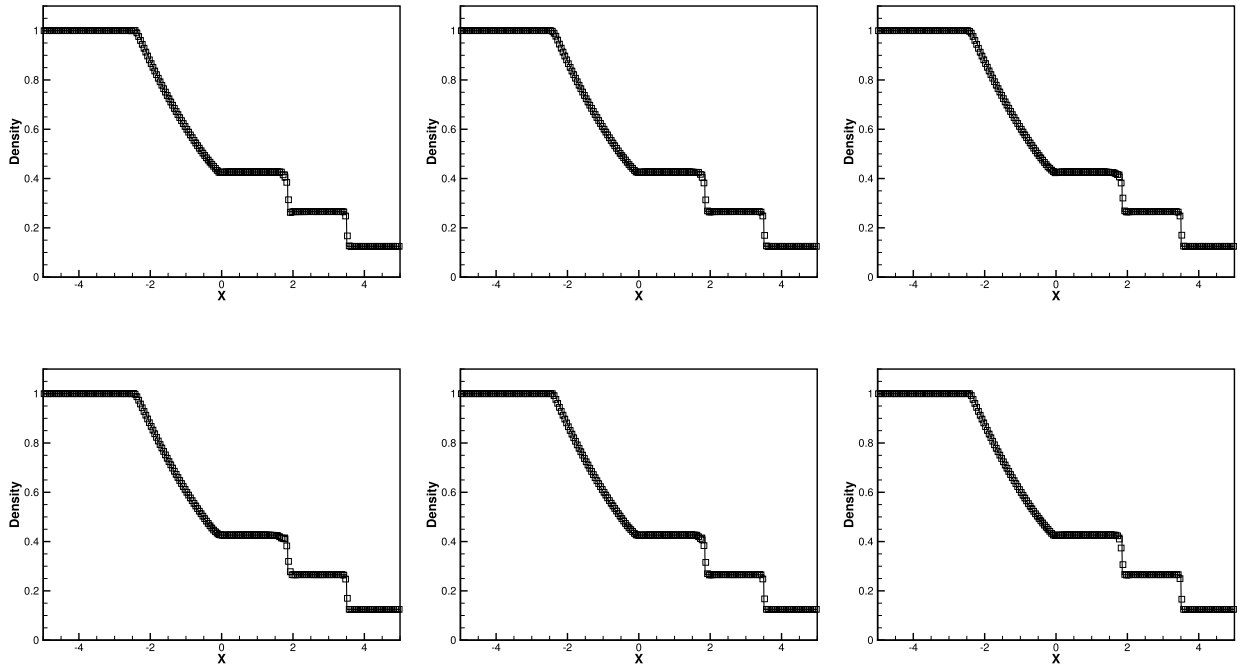
Fig. 3.3. The Sod problem. $t = 2.0$. Top row: new indicator. Bottom row: KXRCF indicator. Left: $k = 2$; middle: $k = 4$; right: $k = 6$. Solid line: the exact solution; Squares: numerical solution. 200 cells. One point per cell is plotted.

Fig. 3.4. The Sod problem. Troubled cells (denoted by squares). Top row: new indicator. Bottom row: KXRCF indicator. Left: $k = 2$; middle: $k = 4$; right: $k = 6$. 200 cells.
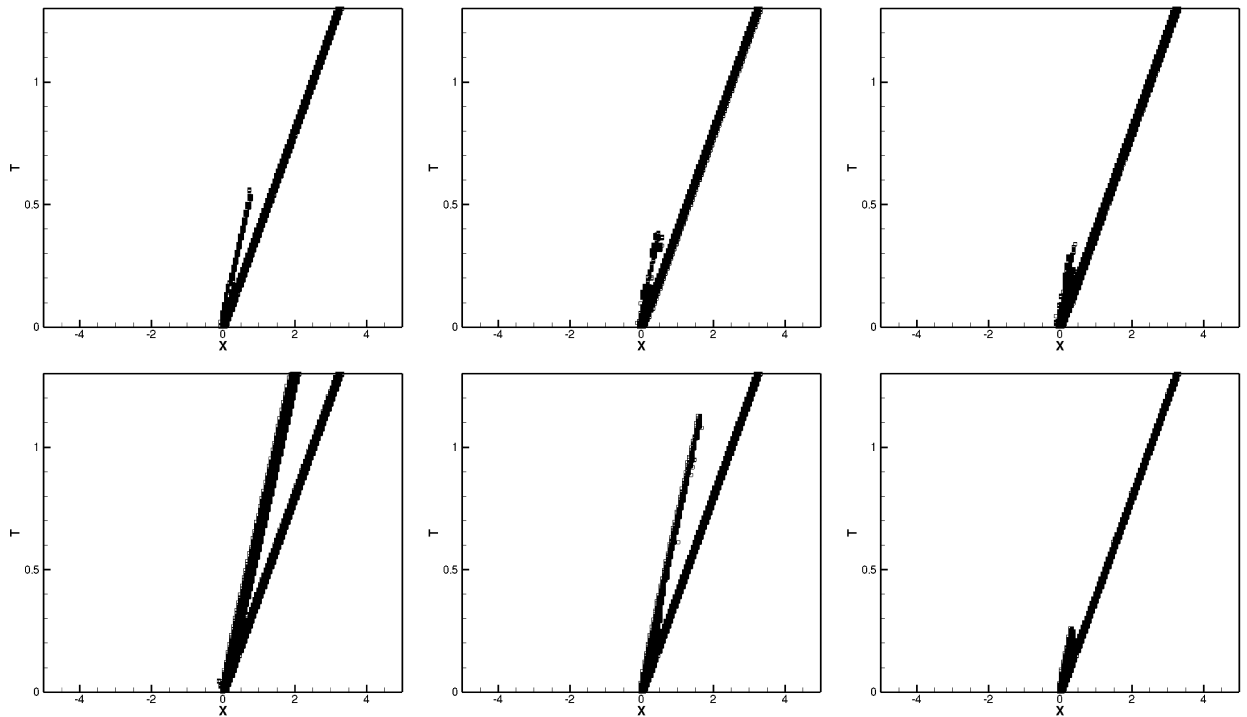
Fig. 3.5. The Lax problem. Troubled cells (denoted by squares). Top row: new indicator. Bottom row: KXRCF indicator. Left: $k = 2$; middle: $k = 4$; right: $k = 6$. 200 cells.

Table 3.2
Average and maximum percentages of cells flagged as troubled cells subject to different troubled-cell indicators for the double rarefaction wave problem.

N	Schemes	$\mathcal{P}_2$		$\mathcal{P}_4$		$\mathcal{P}_6$	
	Indicator	Ave	Max	Ave	Max	Ave	Max
200	new	0.70	6.00	0.93	6.00	3.95	15.00
	KXRCF	37.62	74.00	35.64	63.50	33.57	53.00
400	new	0.18	3.00	0.23	3.00	0.98	7.50
	KXRCF	35.66	71.50	34.95	64.50	33.91	54.00

Table 3.3
Average and maximum percentages of cells flagged as troubled cells subject to different troubled-cell indicators for the LeBlanc problem.

N	Schemes	$\mathcal{P}_2$		$\mathcal{P}_4$		$\mathcal{P}_6$	
	Indicator	Ave	Max	Ave	Max	Ave	Max
300	new	1.55	2.67	1.57	3.67	2.66	5.00
	KXRCF	4.38	8.33	3.76	7.67	3.75	9.33
600	new	0.75	1.33	0.76	1.83	1.06	2.50
	KXRCF	2.79	7.17	2.26	5.50	2.25	5.83

Example 3.3. We use the following Riemann initial condition for the Lax problem:

$$(\rho, v, p) = (0.445, 0.698, 3.528) \text{ for } x \in [-5, 0]; \qquad (\rho, v, p) = (0.5, 0, 0.571) \text{ for } x \in (0, 5].$$

Results similar to the previous example, at $t = 1.3$, are observed. To save space, we only show the time history of the troubled cells for both indicators in Fig. 3.5.

Example 3.4. The double rarefaction wave problem [13]. We use the following Riemann initial condition for the double rarefaction wave problem:

$$(\rho, v, p) = (7, -1, 0.2) \text{ for } x \in [-1, 0]; \qquad (\rho, v, p) = (7, 1, 0.2) \text{ for } x \in (0, 1].$$

This test does not have shocks but negative density/pressure might easily appear. Results similar to the previous examples, at $t = 0.6$, are given in Table 3.2 and in Figs. 3.6–3.7. The new indicator performs better than KXRCF in terms having smaller
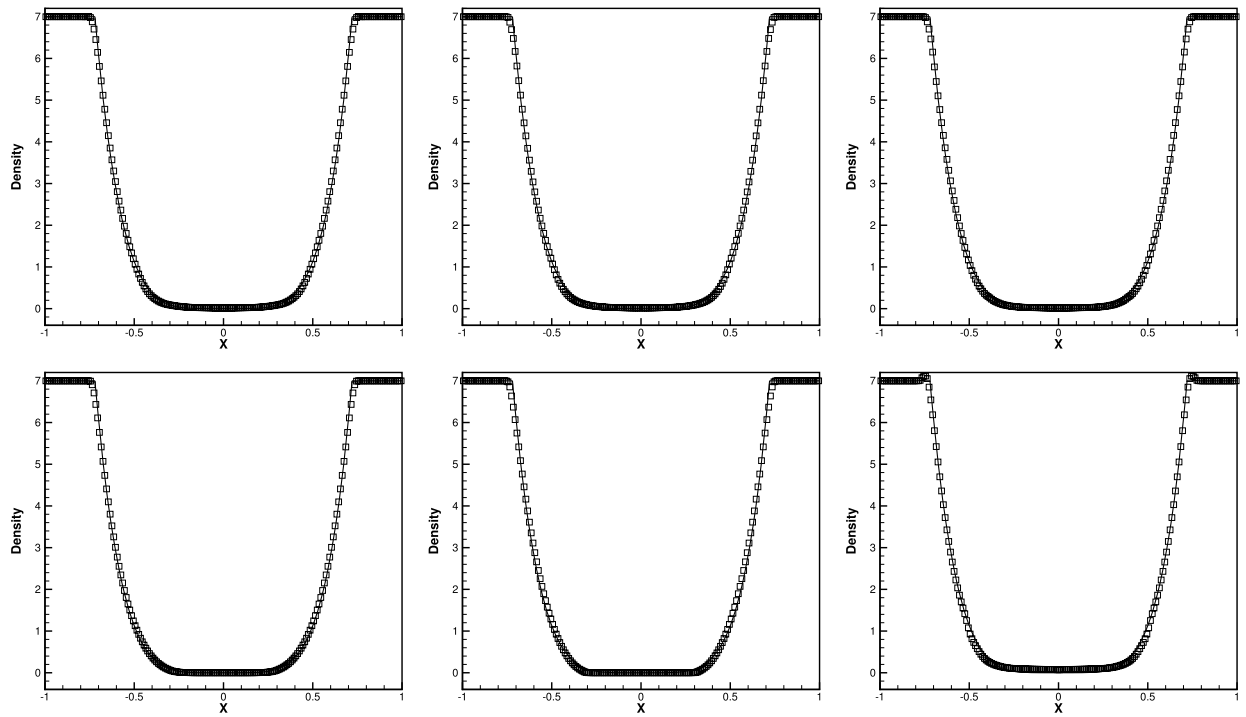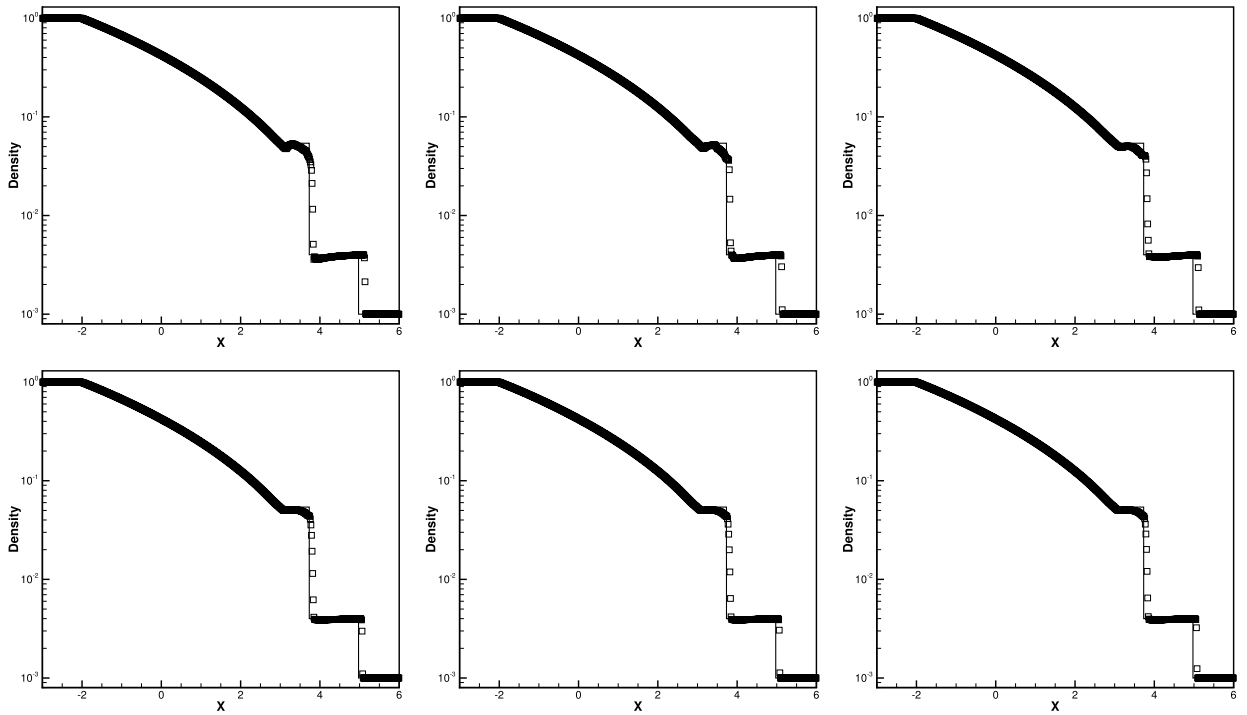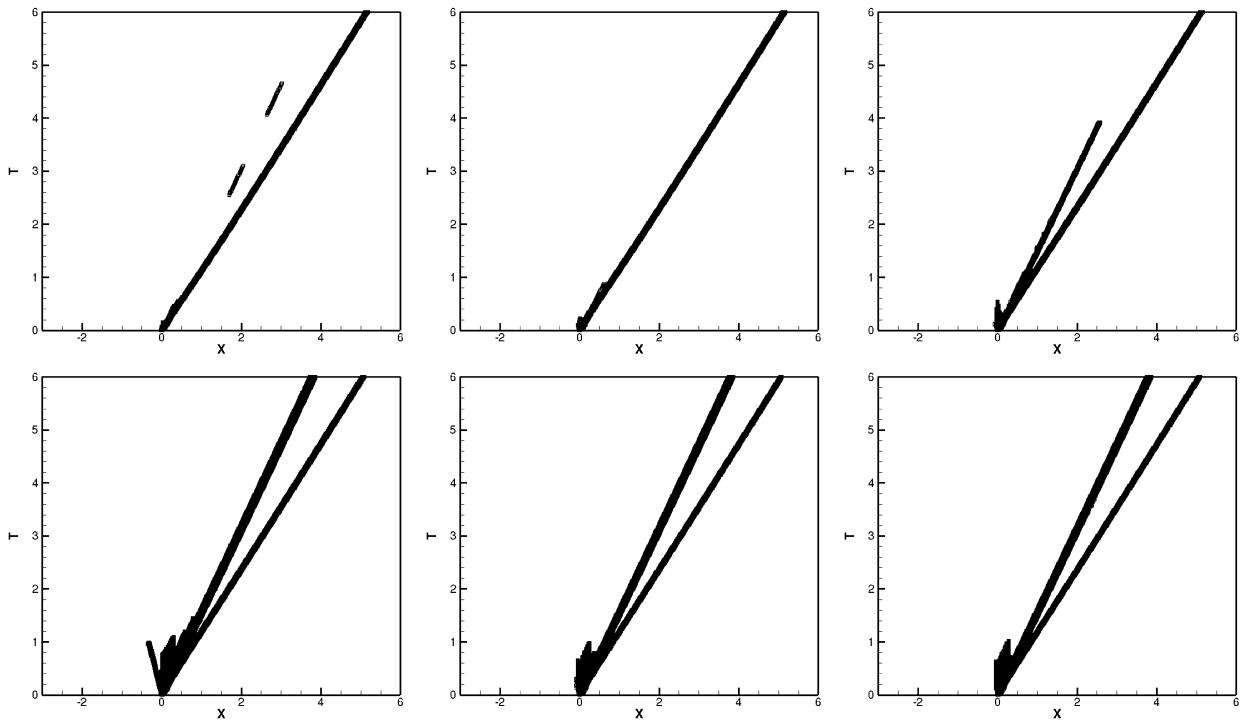
Fig. 3.6. The double rarefaction wave problem. $t = 0.6$. Top row: new indicator. Bottom row: KXRCF indicator. Left: $k = 2$; middle: $k = 4$; right: $k = 6$. Solid line: the exact solution; Squares: numerical solution. 200 cells. One point per cell is plotted.
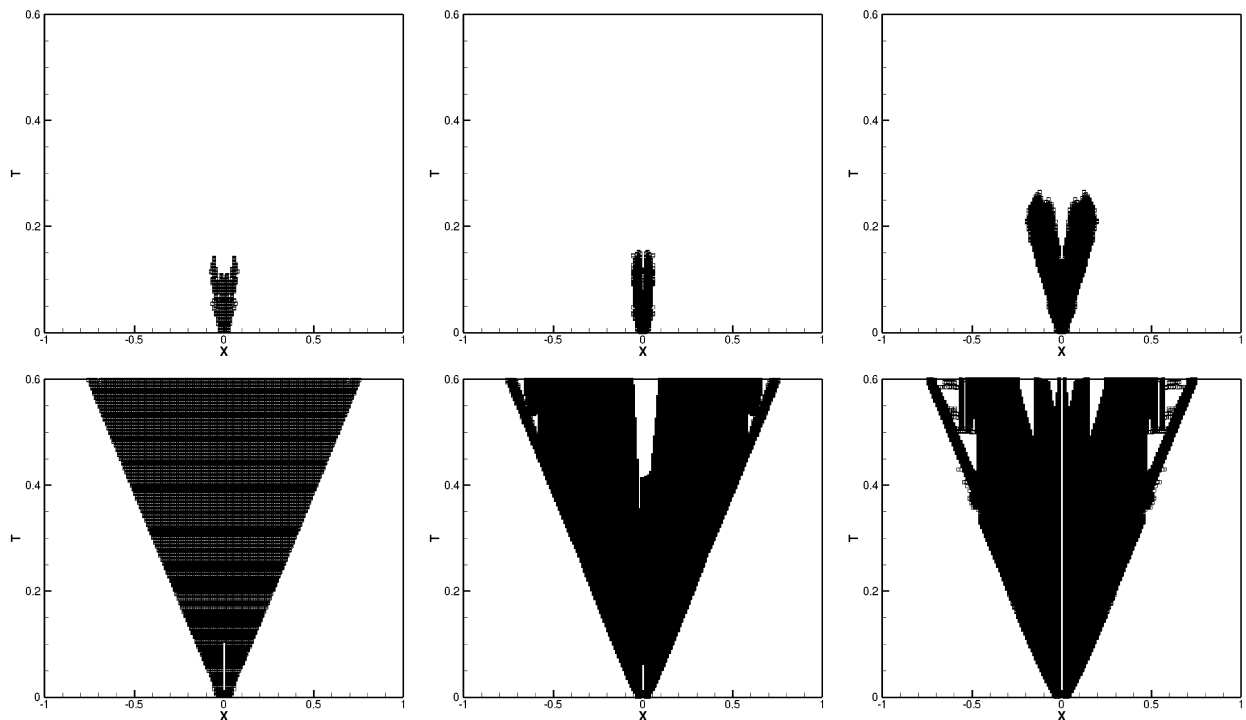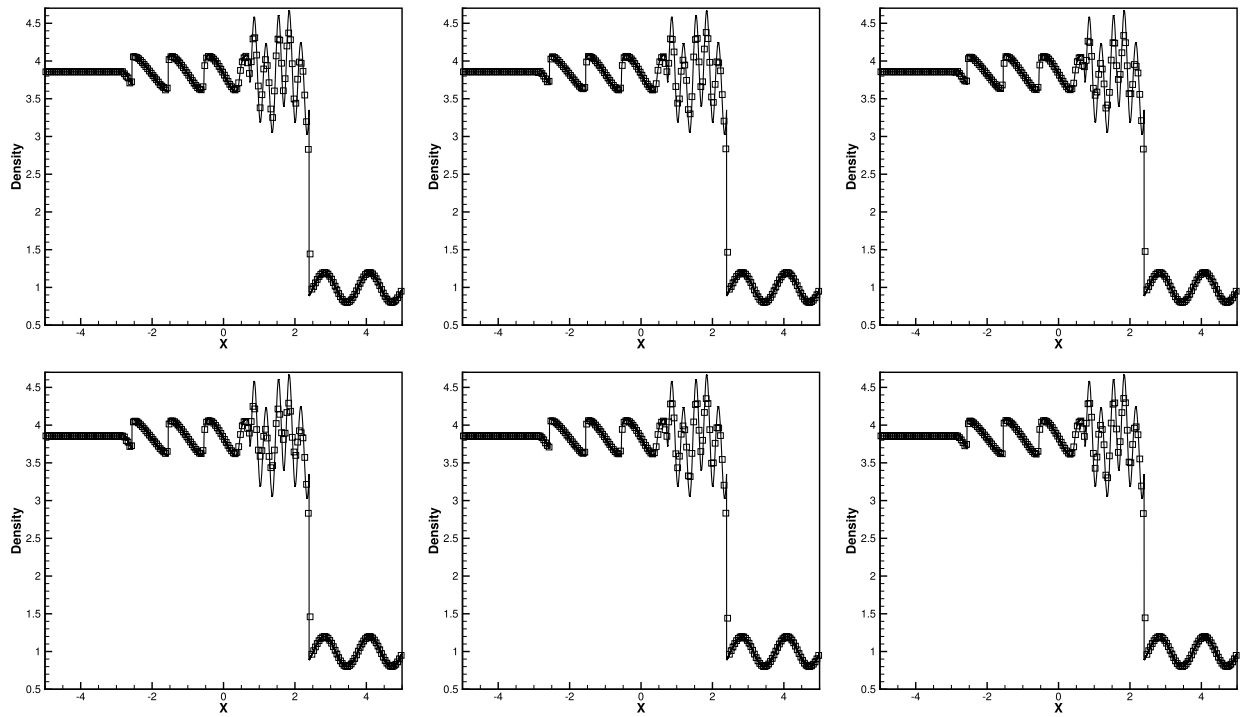

Fig. 3.7. The double rarefaction wave problem. Troubled cells (denoted by squares). Top row: new indicator. Bottom row: KXRCF indicator. Left: $k = 2$; middle: $k = 4$; right: $k = 6$. 200 cells.

Fig. 3.8. The LeBlanc problem. $t = 6.0$. Top row: new indicator. Bottom row: KXRCF indicator. Left: $k = 2$; middle: $k = 4$; right: $k = 6$. Solid line: the exact solution; Squares: numerical solution. 600 cells. One point per cell is plotted.

Fig. 3.9. The LeBlanc problem. Troubled cells (denoted by squares). Top row: new indicator. Bottom row: KXRCF indicator. Left: $k = 2$; middle: $k = 4$; right: $k = 6$. 600 cells.

Fig. 3.10. The Shu–Osher problem. $t = 1.8$. Top row: new indicator. Bottom row: KXRCF indicator. Left: $k = 2$; middle: $k = 4$; right: $k = 6$. Solid line: the exact solution; Squares: numerical solution. 200 cells. One point per cell is plotted.
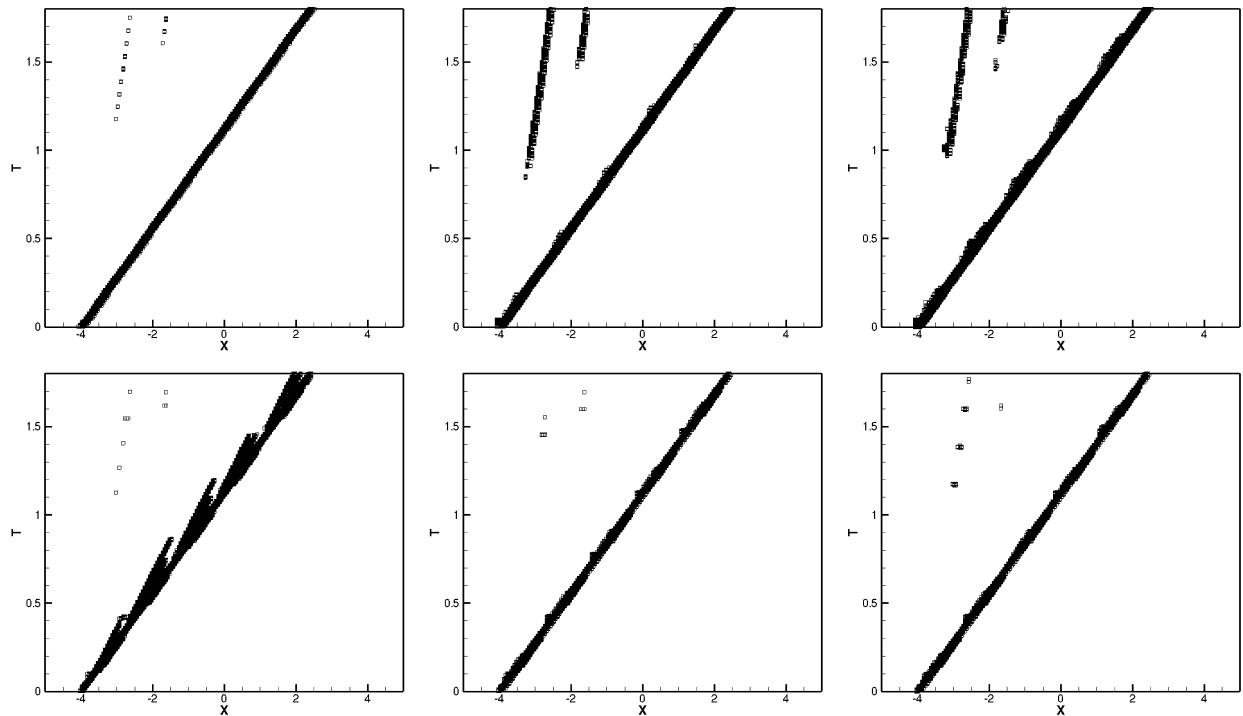
Fig. 3.11. The Shu–Osher problem. Troubled cells (denoted by squares). Top row: new indicator. Bottom row: KXRCF indicator. Left: $k = 2$; middle: $k = 4$; right: $k = 6$. 200 cells.

Table 3.4
Average and maximum percentages of cells flagged as troubled cells subject to different troubled-cell indicators for the Shu–Osher problem.

N	Schemes	$\mathcal{P}_2$		$\mathcal{P}_4$		$\mathcal{P}_6$	
	Indicator	Ave	Max	Ave	Max	Ave	Max
200	new	1.70	2.50	2.25	4.50	2.62	5.00
	KXRCF	2.94	5.00	1.80	3.50	1.66	4.50
400	new	0.85	1.50	1.07	2.25	1.23	2.50
	KXRCF	4.57	8.25	1.49	3.00	1.07	2.75

Table 3.5
Average and maximum percentages of cells flagged as troubled cells subject to different troubled-cell indicators for the blast wave problem.

| N	Schemes	$\mathcal{P}_2$		$\mathcal{P}_4$		$\mathcal{P}_6$	
	Indicator	Ave	Max	Ave	Max	Ave	Max
200	new	4.81	8.00	4.28	7.50	5.27	9.00
	KXRCF	25.71	36.00	20.69	31.50	19.34	30.50
400	new	2.21	4.00	2.03	3.75	2.21	4.50
	KXRCF	20.78	30.25	15.35	23.75	13.59	22.75
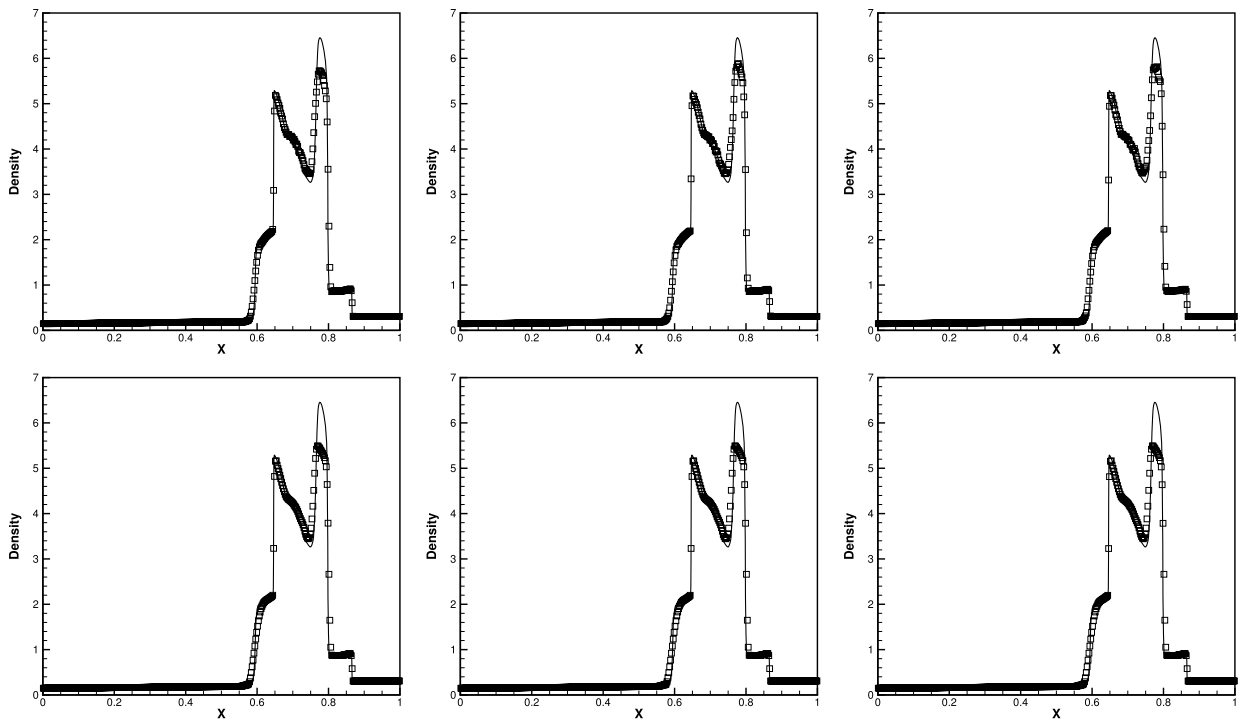
Fig. 3.12. The blast wave problem. $t = 0.038$. Top row: new indicator. Bottom row: KXRCF indicator. Left: $k = 2$; middle: $k = 4$; right: $k = 6$. Solid line: the exact solution; Squares: numerical solution. 400 cells. One point per cell is plotted.

percentage of troubled cells. We specifically mention that the original KXRCF indicator marks even more cells than this modified one for $k = 4, 6$.

Example 3.5. The LeBlanc problem. We use the following Riemann initial condition for the LeBlanc problem:

$$(\rho, v, p) = (1, 0, 0.2/3) \text{ for } x \in [-3, 0]; \qquad (\rho, v, p) = (10^{-3}, 0, 2/3 \times 10^{-10}) \text{ for } x \in (0, 6].$$

γ is taken to be 5/3. We show results at $t = 6.0$ in Table 3.3 and in Figs. 3.8–3.9, and observe a similar pattern as in Example 3.2. Both methods are not able to sharply capture the location of the contact discontinuity and shock due to extreme initial data, with the results for KXRCF indicator slightly better in terms of location of the shock.
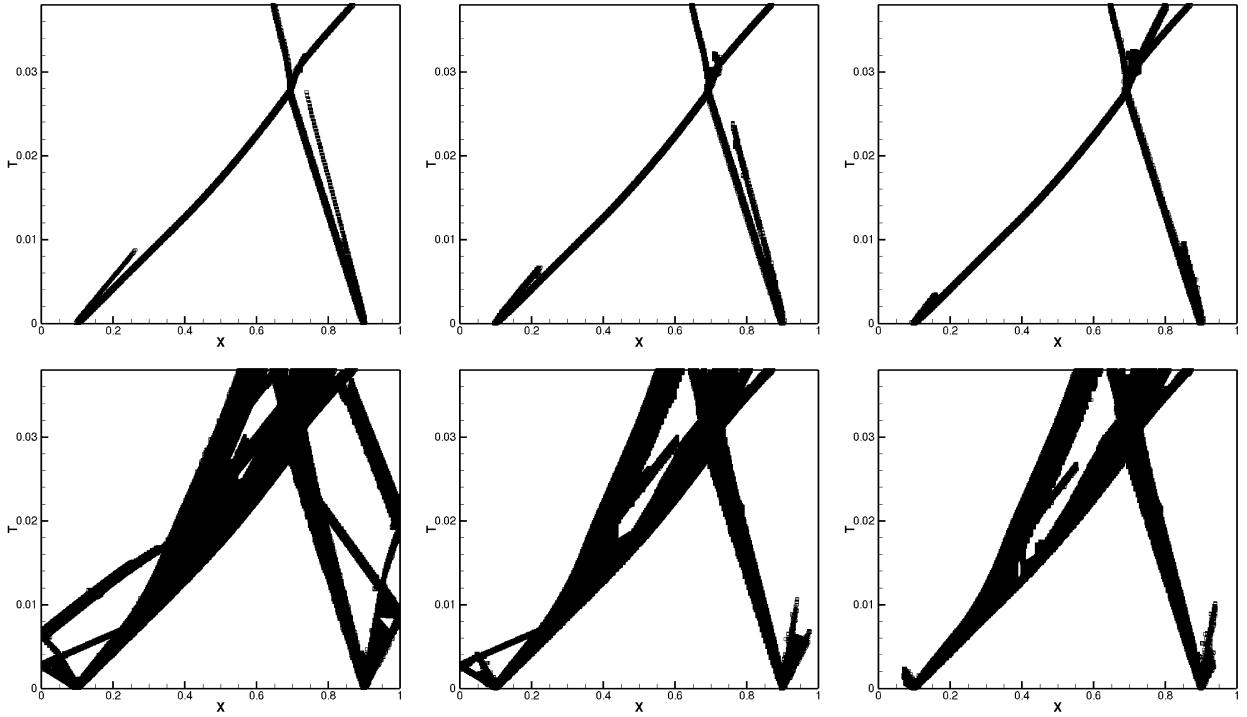
Fig. 3.13. The blast wave problem. Troubled cells (denoted by squares). Top row: new indicator. Bottom row: KXRCF indicator. Left: $k = 2$; middle: $k = 4$; right: $k = 6$. 400 cells.
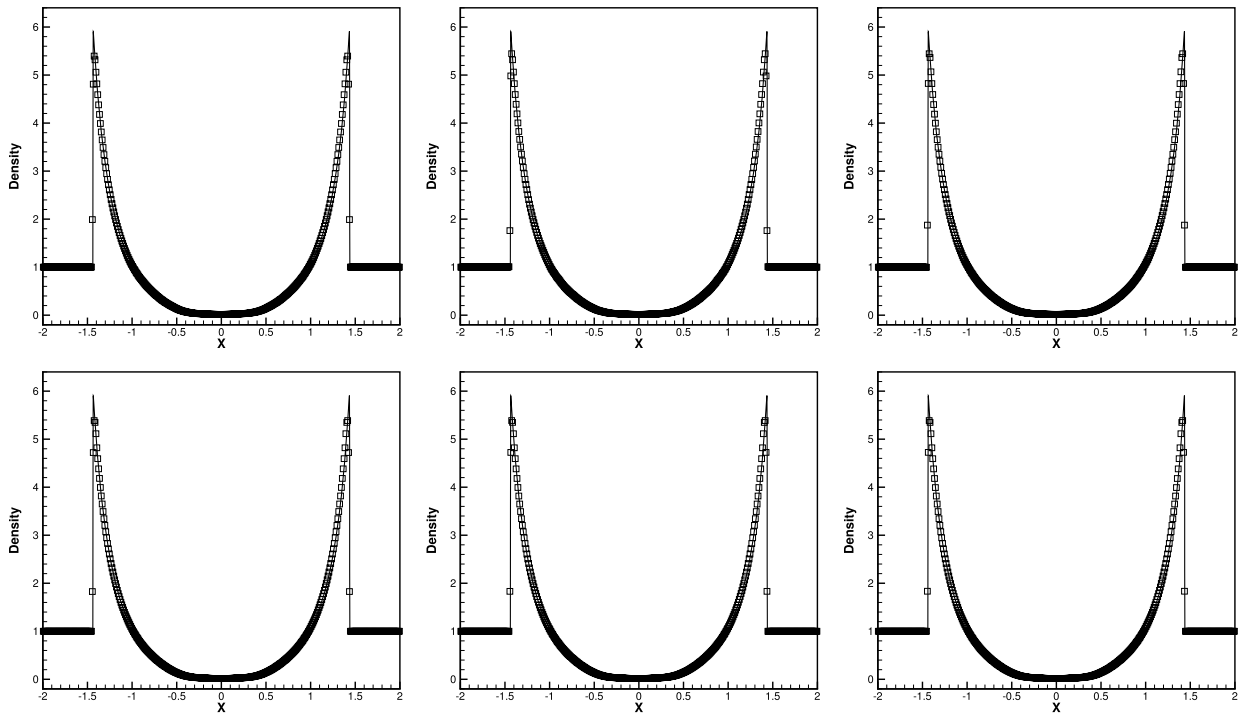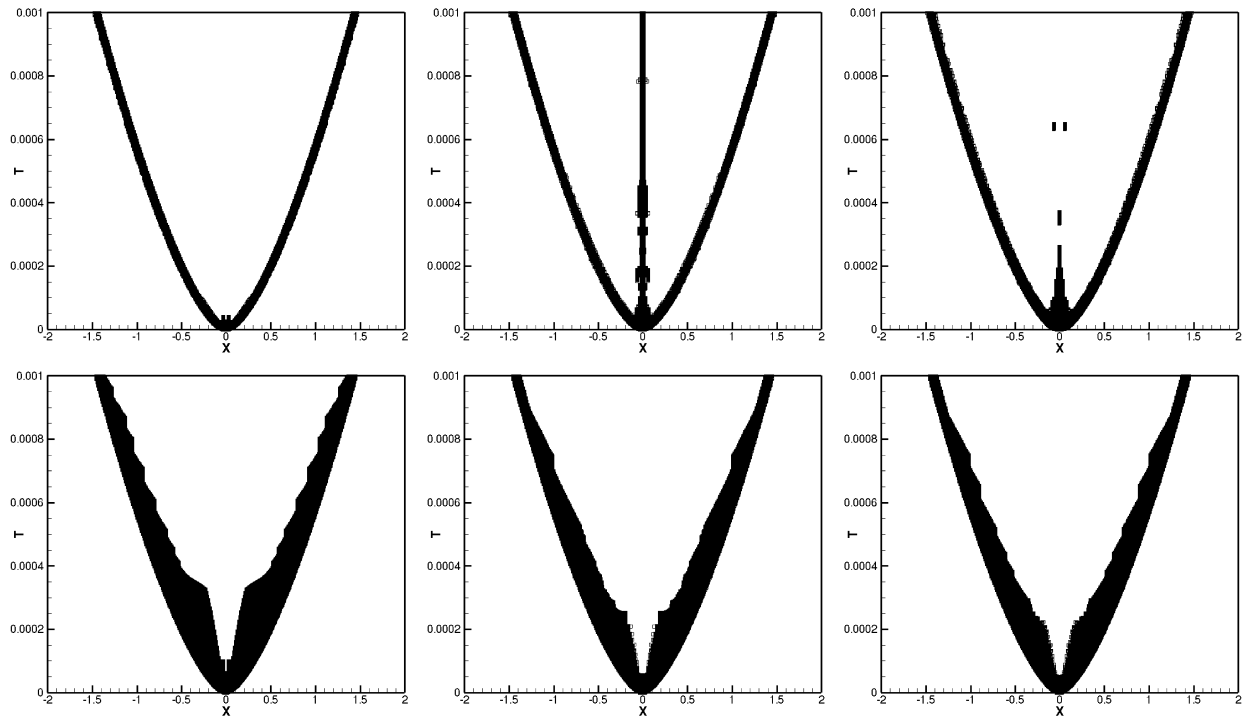

Fig. 3.14. The Sedov blast wave problem. $t = 2.0$. Top row: new indicator. Bottom row: KXRCF indicator. Left: $k = 2$; middle: $k = 4$; right: $k = 6$. Solid line: the exact solution; Squares: numerical solution. 400 cells. One point per cell is plotted.

Table 3.6
Average and maximum percentages of cells flagged as troubled cells subject to different troubled-cell indicators for the Sedov blast wave problem.

N	Schemes	$\mathcal{P}_2$		$\mathcal{P}_4$		$\mathcal{P}_6$	
	Indicator	Ave	Max	Ave	Max	Ave	Max
200	new	6.09	12.00	6.69	12.50	7.04	15.50
	KXRCF	17.21	28.00	14.28	23.00	13.74	22.00
400	new	2.88	6.00	3.07	6.25	2.66	7.75
	KXRCF	12.76	24.00	10.57	20.50	9.92	18.50

Fig. 3.15. The Sedov blast wave problem. Troubled cells (denoted by squares). Top row: new indicator. Bottom row: KXRCF indicator. Left: $k = 2$; middle: $k = 4$; right: $k = 6$. 400 cells.

Table 3.7
Average and maximum percentages of cells flagged as troubled cells subject to different thresholds for the indicator (2.4) for the double Mach reflection problem.

| h	Schemes	$\mathcal{P}_1$		$\mathcal{P}_2$		$\mathcal{P}_3$	
	Threshold	Ave	Max	Ave	Max	Ave	Max
1/120	$C_k = 0.03 \times 2^{k-1}$	0.93	1.25	0.61	0.75	0.62	0.87
	$C_k = 0.015 \times 2^{k-1}$	1.27	1.79	0.91	1.21	0.92	1.31
1/240	$C_k = 0.03 \times 2^{k-1}$	0.46	0.60	0.30	0.37	0.31	0.43
	$C_k = 0.015 \times 2^{k-1}$	0.63	0.90	0.45	0.60	0.46	0.64

Example 3.6. A higher order scheme would show its advantage when the solution contains both shocks and complex smooth regions. A typical example for this is the problem of shock interaction with entropy waves [22]. We solve the Euler equations with a moving Mach = 3 shock interacting with sine waves in density, i.e. initially

$$(\rho, v, p) = (3.857143, 2.629369, 10.333333) \text{ for } x < -4;$$

$$(\rho, v, p) = (1 + 0.2\sin(5x), 0, 1) \text{ for } x \geq -4.$$

The computed density ρ is plotted at $t = 1.8$ against a computed reference "exact" solution on a very fine mesh.

We show results at $t = 1.8$ in Table 3.4 and in Figs. 3.10–3.11, and observe a similar pattern as in the previous example. Here we also notice from Fig. 3.10 that the resolution of the density structure behind the strong shock does not get better for higher order degree approximations. This is expected to be caused by the choice of the low-order minmod-type limiter
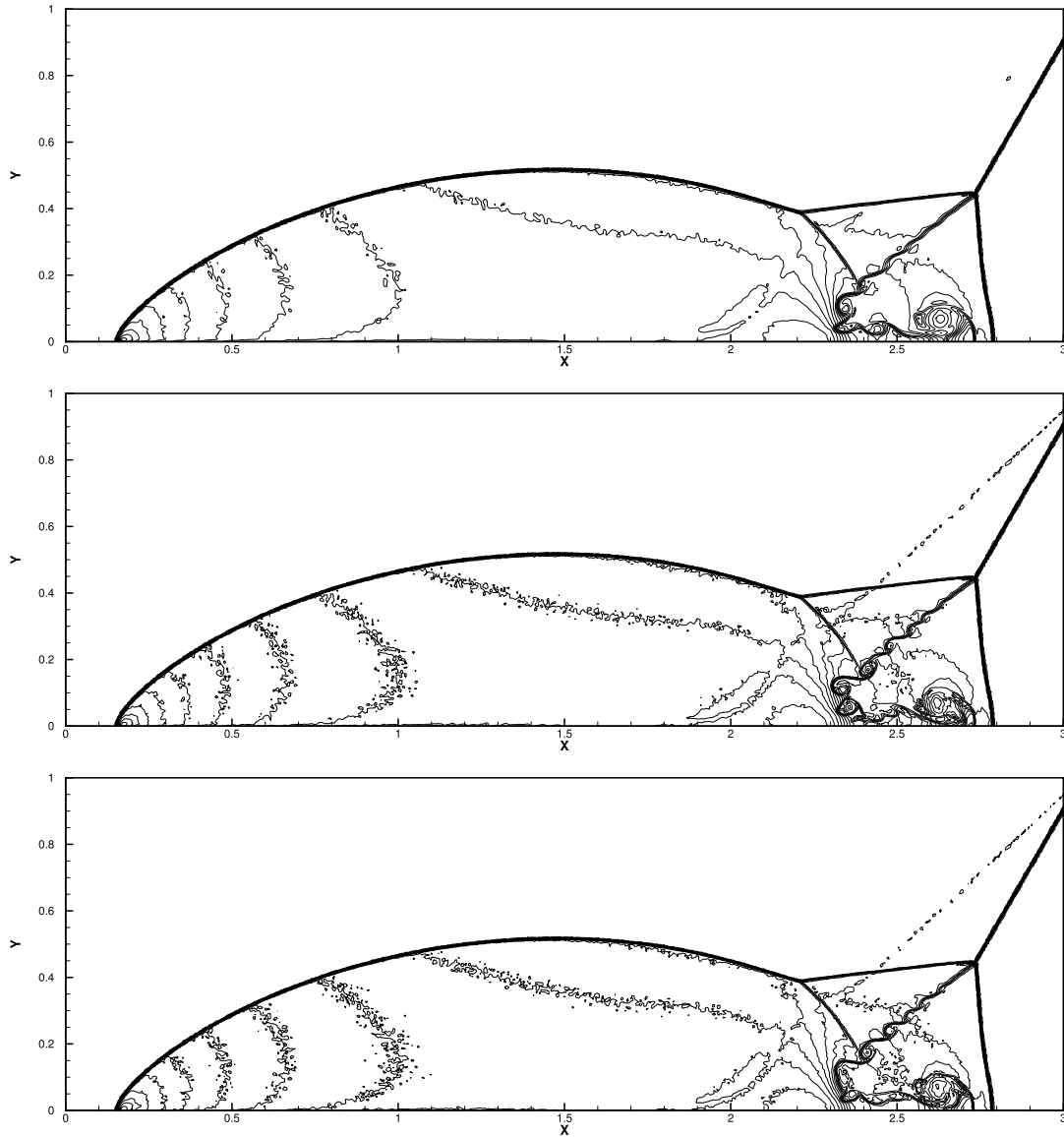
Fig. 3.16. Double Mach refection problem. Top to bottom: second order to fourth order ($k = 1, 2, 3$). 30 equally spaced density contours from 1.5 to 21.5. The mesh points on the boundary are uniformly distributed with cell length $h = 1/240$. The threshold for the troubled-cell indicator (2.4) is $C_k = 0.015 \times 2^{k-1}$.

Table 3.8
Average and maximum percentages of cells flagged as troubled cells subject to different thresholds for the indicator (2.4) for the forward step problem.

h	Schemes	$\mathcal{P}_1$		$\mathcal{P}_2$		$\mathcal{P}_3$	
	Threshold	Ave	Max	Ave	Max	Ave	Max
1/40	$C_k = 0.03 \times 2^{k-1}$	4.44	5.49	2.30	3.04	3.41	4.35
	$C_k = 0.015 \times 2^{k-1}$	7.43	8.94	4.48	5.58	5.36	6.72
1/80	$C_k = 0.03 \times 2^{k-1}$	2.29	2.75	1.16	1.53	1.78	2.28
	$C_k = 0.015 \times 2^{k-1}$	3.91	4.66	2.25	2.78	2.72	3.37

on the troubled cells, since the wave structure behind the strong shock are propagated from the shock, and the same limiter is used for all polynomial degrees on the detected shock cells.

Example 3.7. We consider the interaction of blast waves [27] with the initial conditions:

$$(\rho, v, p) = (1, 0, 1000) \text{ for } 0 \le x < 0.1;$$
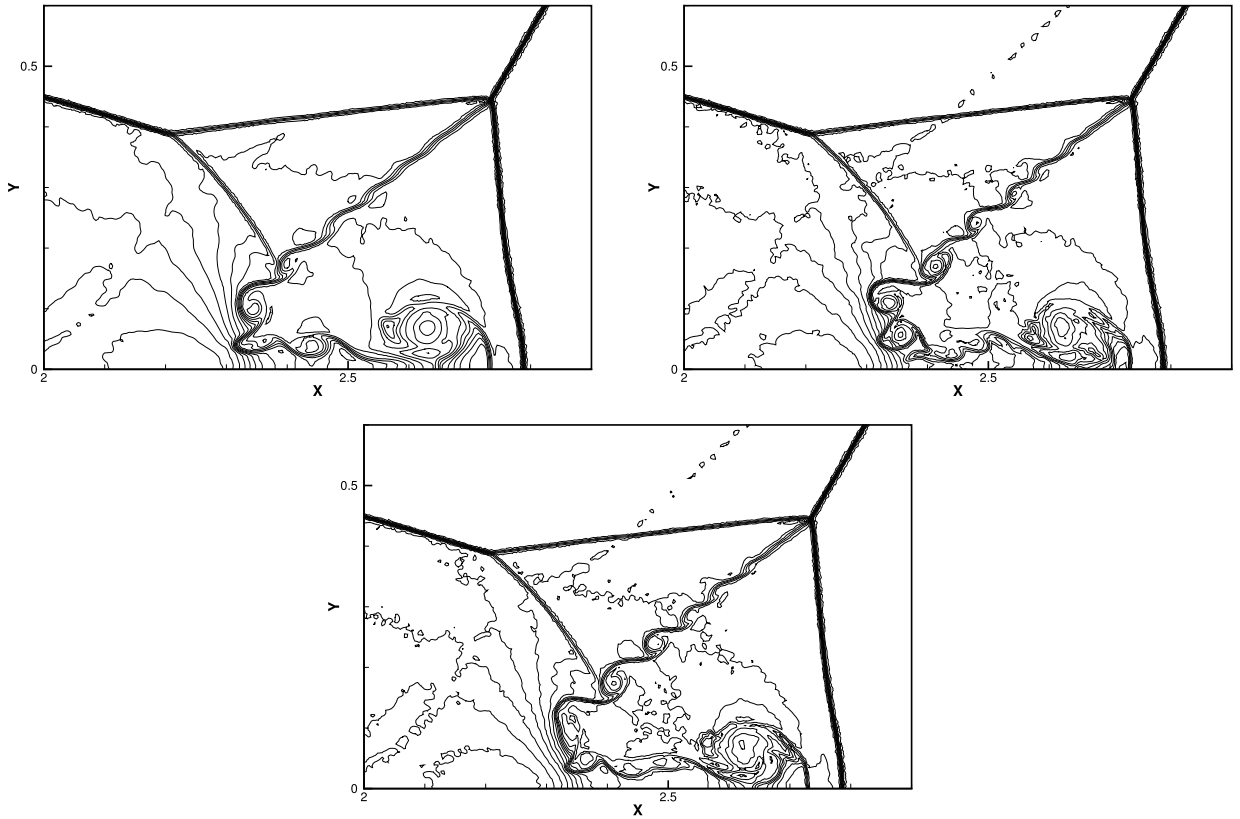
Fig. 3.17. Double Mach refection problem. Top left: $k = 1$; top right: $k = 2$; bottom: $k = 3$. Threshold $C_k = 0.015 \times 2^{k-1}$. Zoom-in pictures around the Mach stem. 30 equally spaced density contours from 1.5 to 21.5. The mesh points on the boundary are uniformly distributed with cell length $h = 1/240$.

$$(\rho, v, p) = (1, 0, 0.01) \text{ for } 0.1 \leq x < 0.9;$$

$$(\rho, v, p) = (1, 0, 100) \text{ for } 0.9 \leq x.$$

A reflecting boundary condition is applied to both ends. The computed density ρ is plotted at $t = 0.038$ against the reference "exact" solution, which is a converged solution computed by the fifth order finite difference WENO scheme [10] with 2000 grid points.

Results similar to the previous examples, at $t = 0.038$, are shown in Table 3.5 and in Figs. 3.12–3.13. The new indicator performs better than the KXRCF indicator in terms of marking fewer troubled cells and giving better resolution. Similar to the previous test, we also notice from Fig. 3.12 that the resolution does not get better for higher order degree approximations, which is expected to be caused by the choice of the low-order minmod-type limiter on the troubled cells.

Example 3.8. The Sedov blast wave problem. This problem contains very low density with strong shocks. The exact solution is specified in detail in [11,19]. The computational domain is $[-2, 2]$ and initial conditions are: $\rho = 1$, $\mu = 0$ and $E = 10^{-12}$ everywhere except that the energy in the center cell is the constant $3200000\triangle x$ (emulating a δ-function at the center). The final computational time is $t = 0.001$.

Results similar to the previous examples, at $t = 0.001$, are shown in Table 3.6 and in Figs. 3.14–3.15. We can observe a similar pattern as the previous tests. The new indicator marks about the same amount of troubled cells (maximum number of troubled cells is $200 \times 12\% = 24$ for $k = 2$, $200 \times 12.5\% = 25$ for $k = 4$, and $200 \times 15.5\% = 31$ for $k = 6$ for both meshes), while the KXRCF tends to mark more cells with a mesh refinement.

3.2. 2D tests

Now, we solve the three 2D compressible Euler tests considered in [7] on unstructured triangular meshes. For the compressible Euler equations in 2D, the conserved variable u and the flux variable f in the conservation laws (1.1) are given as follows:
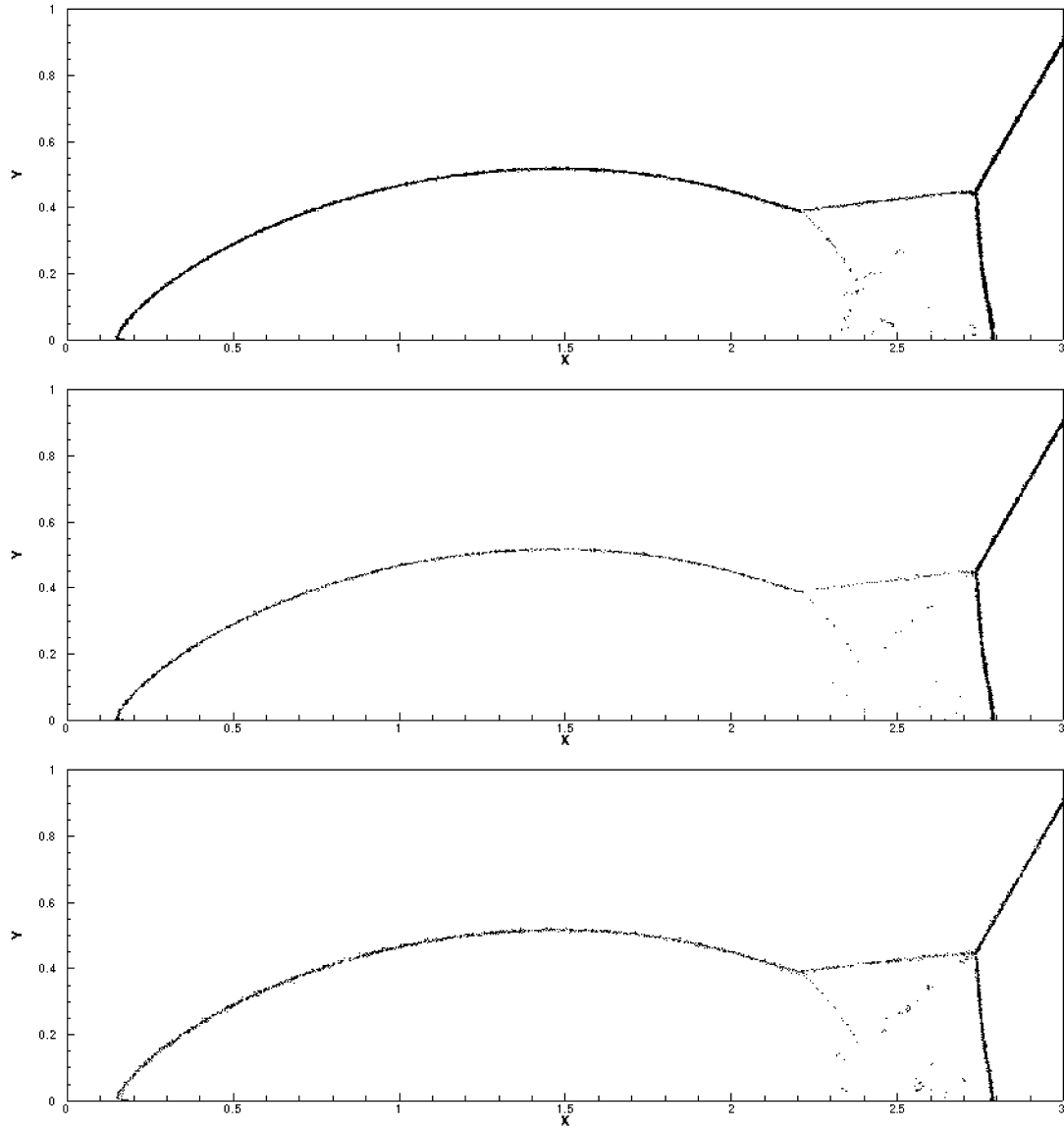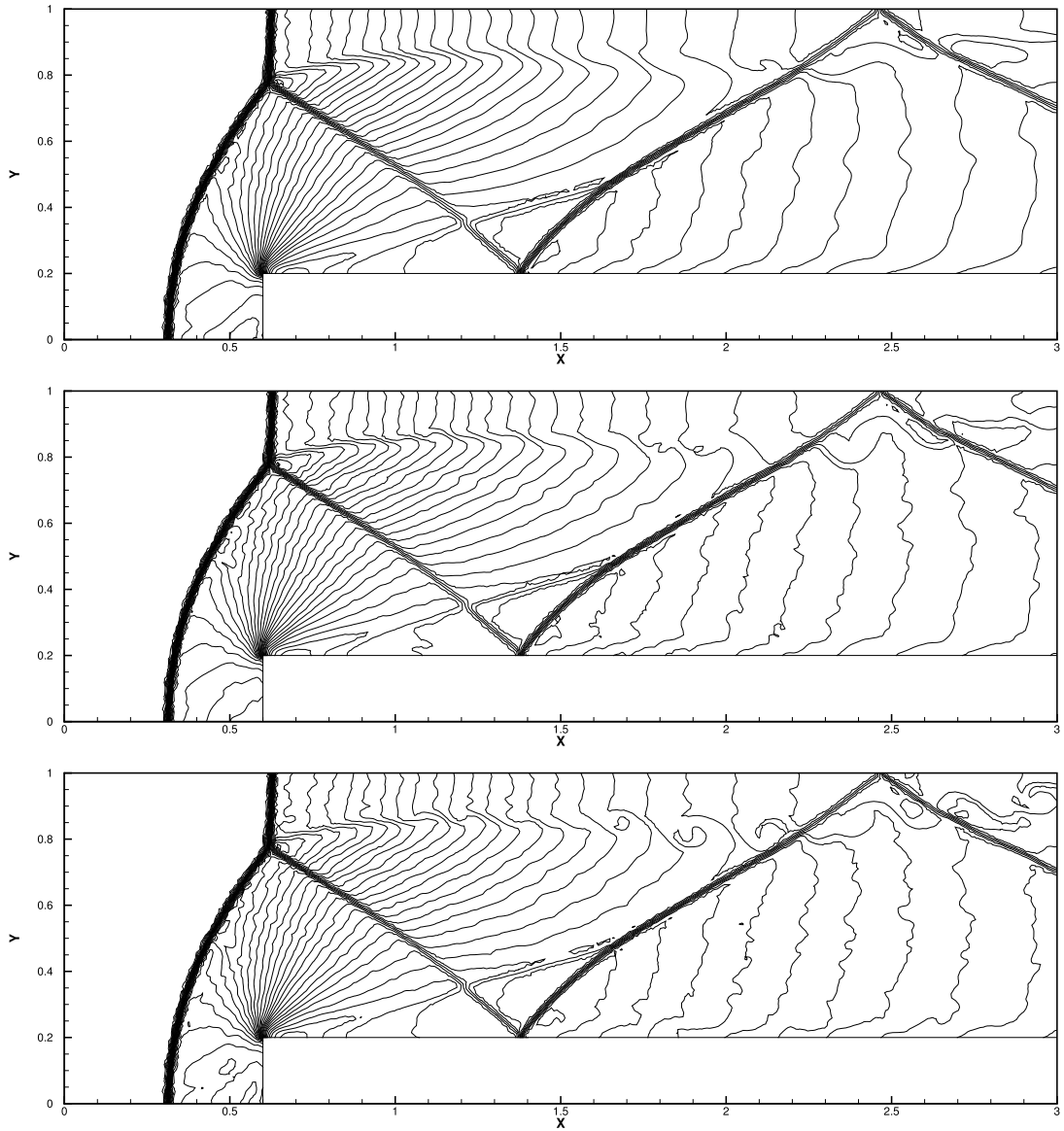
Fig. 3.18. Double Mach refection problem. Top to bottom: second order to fourth order ($k = 1, 2, 3$). Troubled cells are marked black. The mesh points on the boundary are uniformly distributed with cell length $h = 1/240$. The threshold for the troubled-cell indicator (2.4) is $C_k = 0.015 \times 2^{k-1}$.
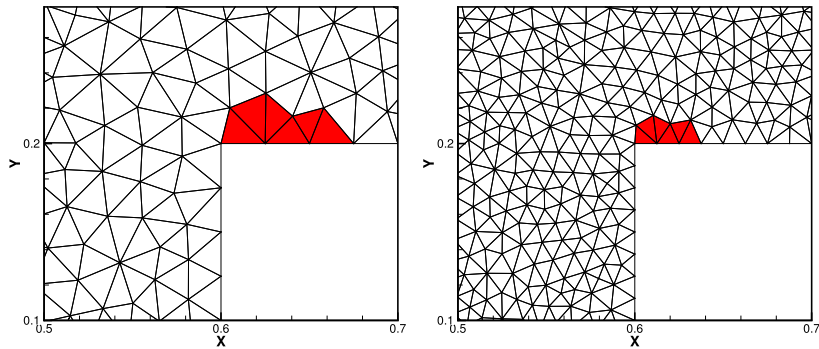
Fig. 3.19. Zoom-in of the computational mesh at the corner. The 6 red cells are flagged for resetting. Left: zoom-in of the mesh with mesh size $h = 1/40$; right: zoom-in of the mesh with mesh size $h = 1/80$. (For interpretation of the references to color in this figure legend, the reader is referred to the web version of this article.)
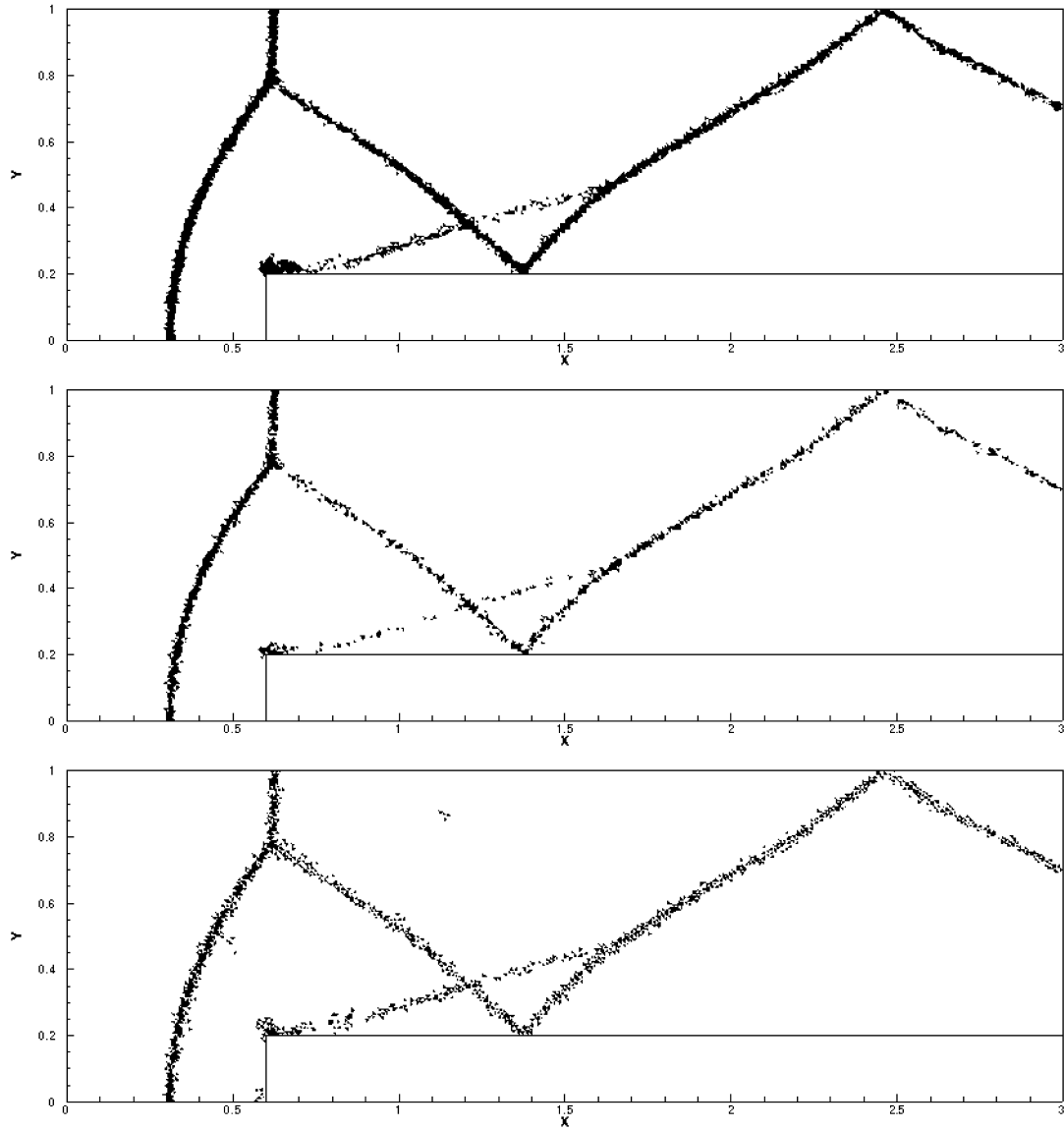
Fig. 3.20. Forward step problem. Top to bottom: second order to fourth order ($k = 1, 2, 3$). 30 equally spaced density contours from 0.32 to 6.15. The mesh points on the boundary are uniformly distributed with cell length $h = 1/80$. The threshold for the troubled-cell indicator (2.4) is $C_k = 0.015 \times 2^{k-1}$.

$$
u = \begin{bmatrix} \rho \\ \rho\mu \\ \rho\nu \\ E \end{bmatrix}, \qquad f = (f_x, f_y) = \left(\begin{bmatrix} \rho\mu \\ \rho\mu^2 + p \\ \rho\mu\nu \\ \mu(E + p) \end{bmatrix}, \begin{bmatrix} \rho\nu \\ \rho\mu\nu \\ \rho\nu^2 + p \\ \nu(E + p) \end{bmatrix} \right),
$$

where ρ is the density, (μ, ν) is the velocity vector, E is the total energy, $p = (\gamma - 1)\left(E - \frac{\rho}{2}(\mu^2 + \nu^2)\right)$ is the pressure and γ is taken to be 1.4 in our test cases.

Here we take the DG polynomial degree to be $k = 1$ (second order), $k = 2$ (third order), or $k = 3$ (fourth order). We compare the percentage of identified troubled cells using the indicator (2.4) with two different choices of the threshold constant, namely, $C_k = 0.03 \times 2^{k-1}$ or $C_k = 0.015 \times 2^{k-1}$. The numerical results using both choices of the threshold constant are similar, so we only present the figures with the threshold constant $C_k = 0.015 \times 2^{k-1}$ to save space. We remark again that the choice of the constant C_k is tuned by numerically testing on the double Mach refection problem Example 3.9 on a coarse mesh. From numerical tests not reported in this paper, we observe that the shock indicator is not sensitive to the constant C_k when it is in the range $0.015 \times 2^{k-1} - 0.03 \times 2^{k-1}$ for $k = 1, 2, 3$. Of course, taking a larger threshold constant leads to slightly fewer detected troubled cells, as can be seen in Tables 3.7–3.9.

Fig. 3.21. Forward step problem. Top to bottom: second order to fourth order ($k = 1, 2, 3$). Troubled cells are marked black. The mesh points on the boundary are uniformly distributed with cell length $h = 1/80$. The threshold for the troubled-cell indicator (2.4) is $C_k = 0.015 \times 2^{k-1}$.

Example 3.9. Double Mach reflection. This problem is originally from [27]. The computational domain for this problem is $[0, 4] \times [0, 1]$. The reflecting wall lies at the bottom, starting from $x = \frac{1}{6}$. Initially a right-moving Mach 10 shock is positioned at $x = \frac{1}{6}$, $y = 0$ and makes a $60°$ angle with the x-axis. For the bottom boundary, the exact post-shock condition is imposed for the part from $x = 0$ to $x = \frac{1}{6}$ and a reflective boundary condition is used for the rest. At the top boundary, the flow values are set to describe the exact motion of a Mach 10 shock. We compute the solution up to $t = 0.2$.

Average (over time) and maximum percentages of cells being flagged as troubled cells for the indicator (2.4) with two difference thresholds C_k, are summarized in Table 3.7 for $t = 0.2$ using two consecutive meshes. The percentages of troubled cell get reduced by about a half with a mesh refinement.

The simulation results using indicator (2.4) with $C_k = 0.015 \times 2^{k-1}$ on the fine mesh with $h = 1/240$ are shown in Fig. 3.16. The "zoom-in" pictures around the double Mach stem to show more details are given in Fig. 3.17. The troubled cells identified at the last time step are shown in Fig. 3.18. The approximations for $k = 2$ and $k = 3$ are better than $k = 1$ around the double Mach stem, but are a bit more oscillatory. There is no significant resolution improvement from $k = 2$ to $k = 3$.

Table 3.9

Average and maximum percentages of cells flagged as troubled cells subject to different thresholds for the indicator (2.4) for the shock diffraction problem.

h	Schemes	$\mathcal{P}_1$		$\mathcal{P}_2$		$\mathcal{P}_3$	
	Threshold	Ave	Max	Ave	Max	Ave	Max
1/20	$C_k = 0.03 \times 2^{k-1}$	1.20	1.97	0.82	1.34	0.74	1.28
	$C_k = 0.015 \times 2^{k-1}$	1.71	2.84	1.22	1.97	1.20	2.00
1/40	$C_k = 0.03 \times 2^{k-1}$	0.60	0.97	0.42	0.67	0.38	0.66
	$C_k = 0.015 \times 2^{k-1}$	0.83	1.40	0.61	1.01	0.61	1.03
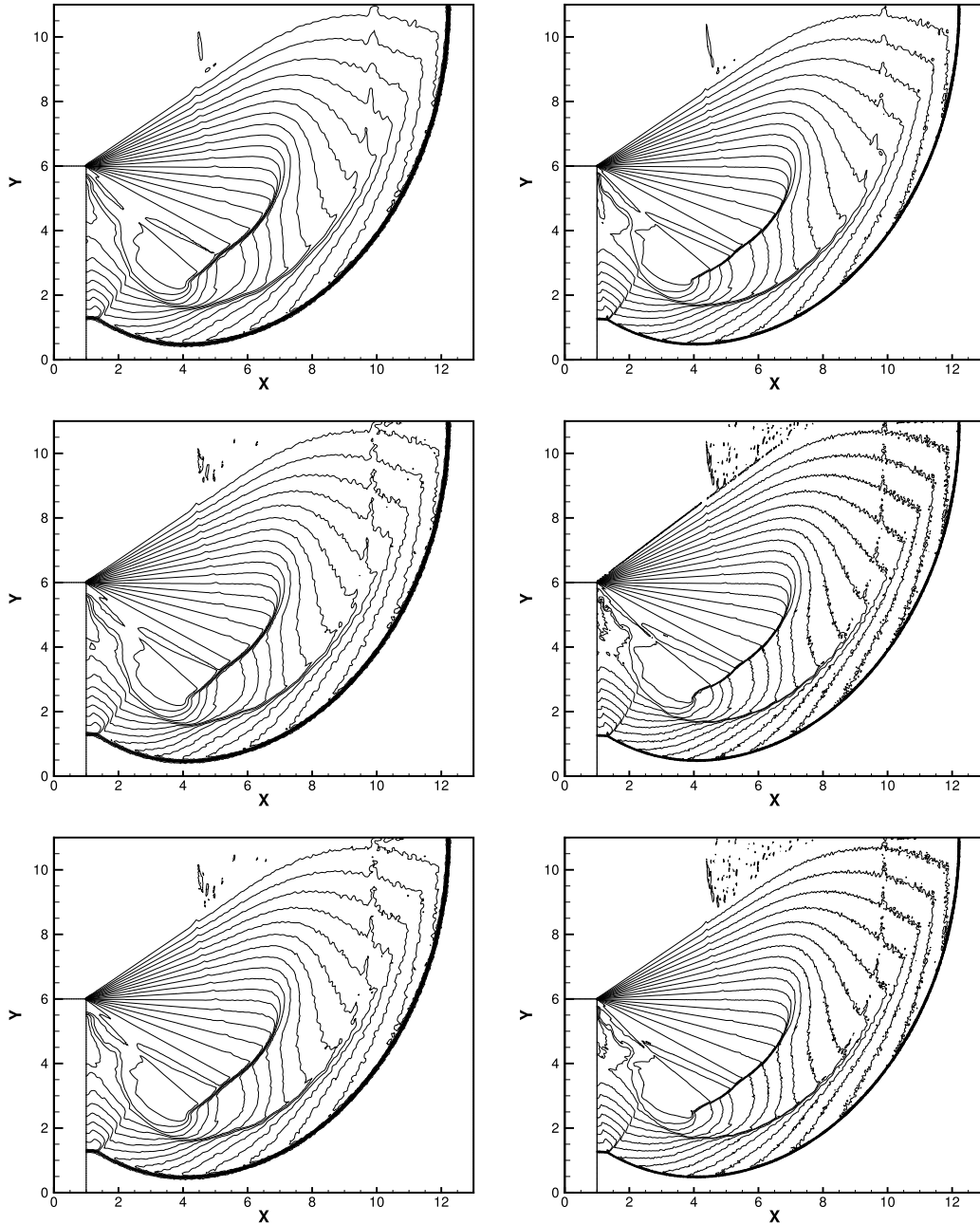
Fig. 3.22. Shock diffraction problem. Top to bottom: second order to fourth order ($k = 1, 2, 3$). Left: coarse mesh, $h = 1/20$; right: fine mesh, $h = 1/40$. Threshold $C_k = 0.015 \times 2^{k-1}$. 20 equally spaced density contours from 0.066227 to 7.0668.
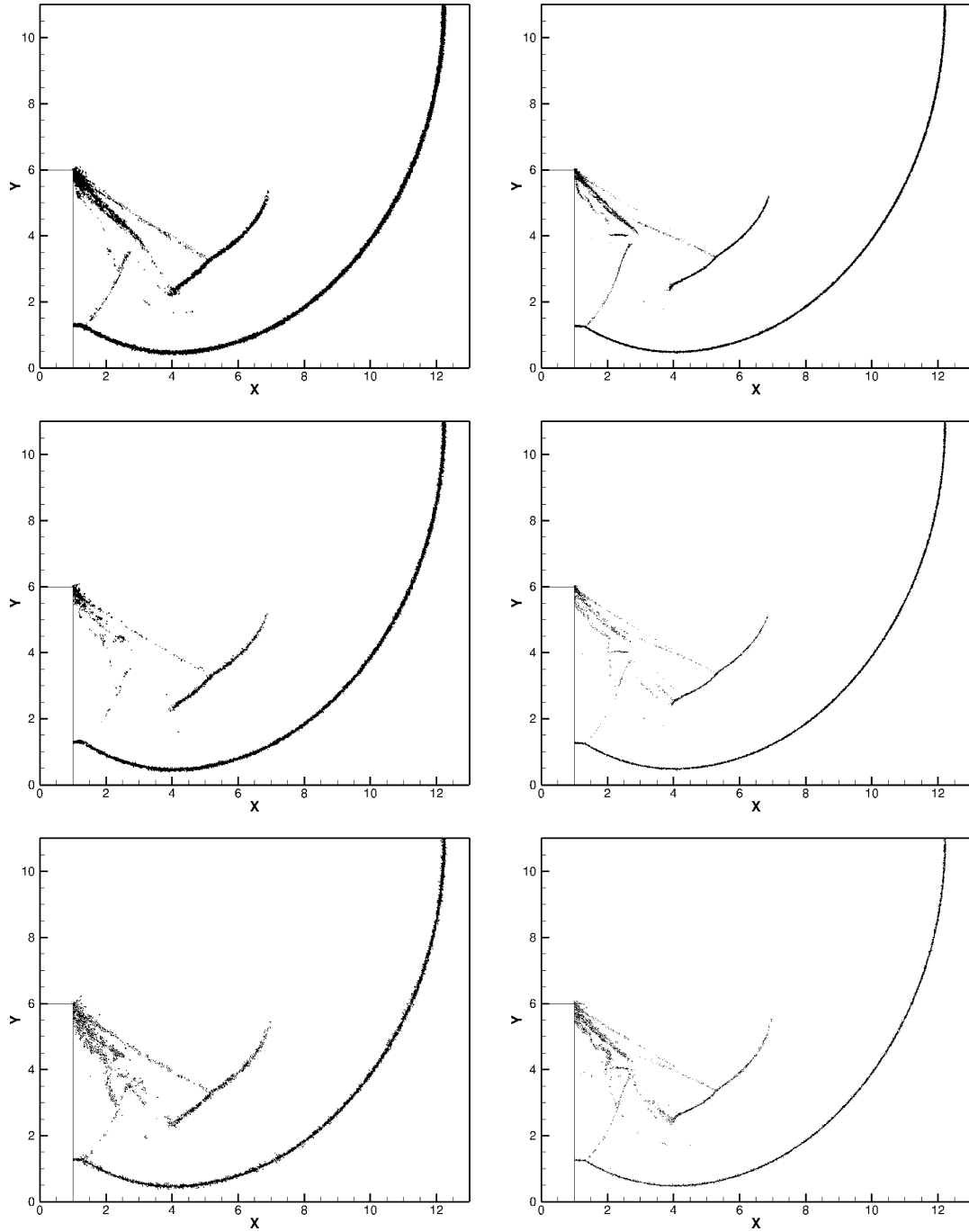
Fig. 3.23. Shock diffraction problem. Top to bottom: second order to fourth order ($k = 1, 2, 3$). Left: coarse mesh, $h = 1/20$; right: fine mesh, $h = 1/40$. Threshold $C_k = 0.015 \times 2^{k-1}$. Troubled cells are marked black.

Example 3.10. A Mach 3 wind tunnel with a step. This model problem is also originally from [27]. The setup of the problem is as follows. The wind tunnel is 1 length unit wide and 3 length units long. The step is 0.2 length units high and is located 0.6 length units from the left-hand end of the tunnel. The problem is initialized by a right-going Mach 3 flow. Reflective boundary conditions are applied along the wall of the tunnel and inflow/outflow boundary conditions are applied at the entrance/exit. The results are shown at $t = 4$.

The corner of the step is a singularity. To avoid an erroneous entropy layer at the downstream bottom wall, we adopt the modification proposed by Woodward and Colella [27] by resetting first 6 cells starting just to the right of the corner of the step, see a "zoom-in" of the reset cells in Fig. 3.19. We keep the solution of these 6 cells as piece-wise constant, with the

same entropy and enthalpy as (the cell average of) the cell just to the left and below the corner of the step by modifying the density and velocity magnitude while keeping pressure cell average fixed.

Average (over time) and maximum percentages of cells being flagged as troubled cells for the indicator (2.4) with two difference thresholds C_k, are summarized in Table 3.8 for $t = 4$ using two consecutive meshes. The percentages of troubled cell get reduced by about a half with a mesh refinement.

The simulation results using indicator (2.4) with $C_k = 0.015 \times 2^{k-1}$ on the mesh with $h = 1/80$ are shown in Fig. 3.20. The troubled cells identified at the last time step are shown in Fig. 3.21. We notice no erroneous Mach stem in Fig. 3.20 due to Woodward and Colella's corner modification.

Example 3.11. Shock passing a backward facing corner (diffraction). The setup of the problem is the following: the computational domain is the union of $[0, 1] \times [6, 11]$ and $[1, 13] \times [0, 11]$; the initial condition is a pure right-moving shock of $Mach = 5.09$, initially located at $x = 0.5$ and $6 \le y \le 11$, moving into undisturbed air ahead of the shock with a density of 1.4 and a pressure of 1. The boundary conditions are inflow at $x = 0, 6 \le y \le 11$, outflow at $x = 13, 0 \le y \le 11$, and Neumann at $1 \le x \le 13$, $y = 0$ and at $0 \le x \le 13$, $y = 11$. No special treatment is done at the corner which is a singularity of the solution. The results are shown at $t = 2.3$.

Average (over time) and maximum percentages of cells being flagged as troubled cells for the indicator (2.4) with two difference thresholds C_k, are summarized in Table 3.9 for $t = 2.3$ using two consecutive meshes. The percentages of troubled cell get reduced by about a half with a mesh refinement.

The simulation results using indicator (2.4) with $C_k = 0.015 \times 2^{k-1}$ on the mesh with $h = 1/20$ and $h = 1/40$ are shown in Fig. 3.22. The troubled cells identified at the last time step are shown in Fig. 3.23.

4. Concluding remarks

In this paper we have introduced a new troubled-cell indicator for the RKDG methods. Extensive one- and two-dimensional simulations on the hyperbolic systems of Euler equations indicate that this new indicator is able to capture shocks without a PDE sensitive parameter to tune. The search for robust high-order limiters on the troubled cells consists of our ongoing work.

References

[1] R. Biswas, K.D. Devine, J.E. Flaherty, Parallel, adaptive finite element methods for conservation laws, Appl. Numer. Math. 14 (1994) 255–283.
[2] A. Burbeau, P. Sagaut, C.-H. Bruneau, A problem-independent limiter for high-order Runge–Kutta discontinuous Galerkin methods, J. Comput. Phys. 169 (2001) 111–150.
[3] B. Cockburn, S. Hou, C.-W. Shu, The Runge–Kutta local projection discontinuous Galerkin finite element method for conservation laws. IV. The multidimensional case, Math. Comput. 54 (1990) 545–581.
[4] B. Cockburn, S.Y. Lin, C.-W. Shu, TVB Runge–Kutta local projection discontinuous Galerkin finite element method for conservation laws. III. One-dimensional systems, J. Comput. Phys. 84 (1989) 90–113.
[5] B. Cockburn, C.-W. Shu, TVB Runge–Kutta local projection discontinuous Galerkin finite element method for conservation laws. II. General framework, Math. Comput. 52 (1989) 411–435.
[6] B. Cockburn, C.-W. Shu, The Runge–Kutta local projection P^1-discontinuous-Galerkin finite element method for scalar conservation laws, RAIRO Modél. Math. Anal. Numér. 25 (1991) 337–361.
[7] B. Cockburn, C.-W. Shu, The Runge–Kutta discontinuous Galerkin method for conservation laws. V. Multidimensional systems, J. Comput. Phys. 141 (1998) 199–224.
[8] M. Dumbser, O. Zanotti, R. Loubère, S. Diot, A posteriori subcell limiting of the discontinuous Galerkin finite element method for hyperbolic conservation laws, J. Comput. Phys. 278 (2014) 47–75.
[9] A. Harten, ENO schemes with subcell resolution, J. Comput. Phys. 83 (1989) 148–184.
[10] G.-S. Jiang, C.-W. Shu, Efficient implementation of weighted ENO schemes, J. Comput. Phys. 126 (1996) 202–228.
[11] L. Korobeinikov, Problems of Point-Blast Theory, American Institute of Physics, 1991.
[12] L. Krivodonova, J. Xin, J.-F. Remacle, N. Chevaugeon, J.E. Flaherty, Shock detection and limiting with discontinuous Galerkin methods for hyperbolic conservation laws, Appl. Numer. Math. 48 (2004) 323–338.
[13] T. Linde, P.L. Roe, Robust Euler codes, in: 13th Computational Fluid Dynamics Conference, AIAA Paper-97-2098.
[14] J. Qiu, C.-W. Shu, Hermite WENO schemes and their application as limiters for Runge–Kutta discontinuous Galerkin method: one-dimensional case, J. Comput. Phys. 193 (2004) 115–135.
[15] J. Qiu, C.-W. Shu, A comparison of troubled-cell indicators for Runge–Kutta discontinuous Galerkin methods using weighted essentially nonoscillatory limiters, SIAM J. Sci. Comput. 27 (2005) 995–1013.
[16] J. Qiu, C.-W. Shu, Hermite WENO schemes and their application as limiters for Runge–Kutta discontinuous Galerkin method. II. Two dimensional case, Comput. Fluids 34 (2005) 642–663.
[17] J. Qiu, C.-W. Shu, Runge–Kutta discontinuous Galerkin method using WENO limiters, SIAM J. Sci. Comput. 26 (2005) 907–929.
[18] W.H. Reed, T.R. Hill, Triangular Mesh Methods for the Neutron Transport Equation, Tech. Report LA-UR-73-479, Los Alamos Scientific Laboratory, Los Alamos, NM, 1973.
[19] L.I. Sedov, Similarity and Dimensional Methods in Mechanics, Translation by Morris Friedman (translation edited by Maurice Holt), Academic Press, New York–London, 1959.
[20] C.-W. Shu, TVB uniformly high-order schemes for conservation laws, Math. Comput. 49 (1987) 105–121.
[21] C.-W. Shu, S. Osher, Efficient implementation of essentially nonoscillatory shock-capturing schemes, J. Comput. Phys. 77 (1988) 439–471.
[22] C.-W. Shu, S. Osher, Efficient implementation of essentially nonoscillatory shock-capturing schemes, II, J. Comput. Phys. 83 (1989) 32–78.
[23] J.M. Tukey, Exploratory Data Analysis, Behavioral Science: Quantitative Methods, 1st ed., Addison-Wesley, 1977.
[24] M.J. Vuik, J.K. Ryan, Multiwavelet troubled-cell indicator for discontinuity detection of discontinuous Galerkin schemes, J. Comput. Phys. 270 (2014) 138–160.

[25] M.J. Vuik, J.K. Ryan, Automated parameters for troubled-cell indicators using outlier detection, SIAM J. Sci. Comput. 38 (2016) A84–A104.
[26] C. Wang, X. Zhang, C.-W. Shu, J. Ning, Robust high order discontinuous Galerkin schemes for two-dimensional gaseous detonations, J. Comput. Phys. 231 (2012) 653–665.
[27] P. Woodward, P. Colella, The numerical simulation of two-dimensional fluid flow with strong shocks, J. Comput. Phys. 54 (1984) 115–173.
[28] X. Zhang, On positivity-preserving high order discontinuous Galerkin schemes for compressible Navier–Stokes equations, J. Comput. Phys. 328 (2017) 301–343.
[29] X. Zhang, C.-W. Shu, On maximum-principle-satisfying high order schemes for scalar conservation laws, J. Comput. Phys. 229 (2010) 3091–3120.
[30] X. Zhang, C.-W. Shu, On positivity-preserving high order discontinuous Galerkin schemes for compressible Euler equations on rectangular meshes, J. Comput. Phys. 229 (2010) 8918–8934.
[31] X. Zhang, C.-W. Shu, Maximum-principle-satisfying and positivity-preserving high-order schemes for conservation laws: survey and new developments, Proc. R. Soc., Math. Phys. Eng. Sci. 467 (2011) 2752–2776.
[32] X. Zhang, Y. Xia, C.-W. Shu, Maximum-principle-satisfying and positivity-preserving high order discontinuous Galerkin schemes for conservation laws on triangular meshes, J. Sci. Comput. 50 (2012) 29–62.
[33] X. Zhong, C.-W. Shu, A simple weighted essentially nonoscillatory limiter for Runge–Kutta discontinuous Galerkin methods, J. Comput. Phys. 232 (2013) 397–415.
[34] J. Zhu, J. Qiu, C.-W. Shu, M. Dumbser, Runge–Kutta discontinuous Galerkin method using WENO limiters. II. Unstructured meshes, J. Comput. Phys. 227 (2008) 4330–4353.
[35] J. Zhu, X. Zhong, C. Shu, J. Qiu, Runge–Kutta discontinuous Galerkin method with a simple and compact Hermite WENO limiter on unstructured meshes, Commun. Comput. Phys. 21 (3) (2017) 623–649, http://dx.doi.org/10.4208/cicp.221015.160816a.
[36] J. Zhu, X. Zhong, C.-W. Shu, J. Qiu, Runge–Kutta discontinuous Galerkin method using a new type of WENO limiters on unstructured meshes, J. Comput. Phys. 248 (2013) 200–220.
[37] J. Zhu, X. Zhong, C.-W. Shu, J. Qiu, Runge–Kutta discontinuous Galerkin method with a simple and compact Hermite WENO limiter, Commun. Comput. Phys. 19 (2016) 944–969.